Robust effects of cortical feedback on thalamic firing mode during naturalistic stimulation

Martin A. Spacek[a,*], Gregory Born[a,b], Davide Crombie[a,b], Steffen Katzner[a,1], Laura Busse[a,c,1,*]

[a] *Division of Neurobiology, Department Biology II, LMU Munich, Munich, Germany*
[b] *Graduate School of Systemic Neuroscience, LMU Munich, Munich, Germany*
[c] *Bernstein Centre for Computational Neuroscience, Munich, Germany*

Abstract

Neurons in the dorsolateral geniculate nucleus (dLGN) of the thalamus are contacted by a large number of feedback synapses from cortex, whose role in visual processing is poorly understood. Past studies investigating this role have mostly used simple visual stimuli and anesthetized animals, but corticothalamic (CT) feedback might be particularly relevant during processing of complex visual stimuli, and its effects might depend on behavioral state. Here, we find that CT feedback robustly modulates responses to naturalistic movie clips by increasing response gain and promoting tonic firing mode. Compared to these robust effects for naturalistic movies, CT feedback effects were less consistent for simple grating stimuli. Finally, while CT feedback and locomotion affected dLGN responses in similar ways, we found their effects to be largely independent. We propose that CT feedback and behavioral state use separate routes to powerfully modulate visual information on its way to cortex.

Keywords: primary visual cortex, lateral geniculate nucleus, feedback, naturalistic movies, locomotion, behavioral state, tonic mode, burst mode

Introduction

Mammalian vision is based on a hierarchy of processing stages that are connected by feedforward circuits projecting from lower to higher levels, and by feedback circuits projecting from higher to lower levels. Feedforward processing is thought to create feature selectivity [1, 2] and invariance to translation, scale, or rotation [2–5], to ultimately enable object recognition [6]. Hypotheses about the functional role of feedback circuits include top-down attention, working memory, prediction, and awareness [7–12]. Compared to theories of feedforward processing, however, there is little consensus on the specific function of feedback connections [13, 14].

Feedback in the visual system targets brain areas as early as the dorsolateral geniculate nucleus (dLGN) of the thalamus, where up to 30% of synaptic connections onto relay cells are established by corticothalamic (CT) feedback [15]. Direct corticogeniculate feedback is

*Correspondence: nature@mspacek.mm.st (MAS), busse@bio.lmu.de (LB)
[1]Senior authors

thought to arise from V1 layer 6 (L6) CT pyramidal cells [16, 17], whose role in visual processing has remained elusive for a number of reasons. L6 CT pyramidal cells have notoriously low firing rates [18–23] and their deep location within cortex makes them a difficult target for *in-vivo* single cell functional imaging [24] and cell-type specific manipulations using optogenetics [25]. L6 CT pyramidal cells are also challenging to identify in extracellular recordings due to the heterogeneity of L6 neurons [16]. The action of CT feedback on dLGN activity is generally considered modulatory rather than driving [26], as CT feedback inputs contact the distal dendrites of relay cells via mGluR1 metabotropic receptors [27], implying rather slow and long-lasting effects on dLGN processing. Since L6 CT pyramidal cells provide both direct excitation and indirect inhibition of dLGN via the thalamic reticular nucleus (TRN) and dLGN inhibitory interneurons [17, 28], the effects of CT feedback are expected to be complex [29].

Despite the massive number of CT inputs to dLGN, the functional impact of corticogeniculate feedback remains unclear [30, 31]. In the literature, diverse methods of manipulation with different temporal scales, specificity and overall sign (activation vs. suppression), have yielded diverse and even conflicting results. CT feedback, for instance, has been shown to modulate geniculate spatial integration [32–39], temporal processing [37, 40], response gain [38, 41–43], and transitions between tonic and burst firing modes [44, 45]. Other studies, however, found that manipulation of CT feedback did not change some or any of these dLGN response properties [25, 37, 46–48].

Most of these previous studies have probed the effects of CT feedback with artificial stimuli, and mostly in anesthetized animals; CT feedback, however, might be most relevant for processing of dynamic naturalistic information and during wakefulness. Indeed, it has previously been suggested that corticogeniculate feedback might be more engaged for moving compared to stationary stimuli [17], and for complex dynamic noise textures than simple moving bars [49], consistent with a potential role in figure-ground processing [50]. Furthermore, since the responsiveness of feedback projections [51], including those originating from V1 corticogeniculate neurons [31], seem to be affected by anesthesia, CT feedback effects should be more evident in alert compared to anesthetized animals.

Here, we recorded spiking activity in dLGN of awake mice and investigated how CT feedback affected dLGN responses to naturalistic movie clips. In order to achieve reliable, temporally precise, and reversible suppression of CT feedback, we conditionally expressed channelrhodopsin2 (ChR2) in V1 parvalbumin-positive (PV+) inhibitory interneurons, whose activation can reliably suppress cortical output [41, 52]. We found that V1 suppression had consistent modulatory effects on dLGN responses to movie clips, which could be captured by divisive transformations. Effects of CT feedback on dLGN responses to grating stimuli were more diverse, likely because their periodicity interacted with mechanisms controlling dLGN firing mode. Finally, while geniculate responses during CT feedback suppression resembled those during low arousal, we found effects of CT feedback and behavioral state to be largely independent. Overall, our results demonstrate that visual information en route to cortex can be reliably modulated by extra-retinal influences such as cortical feedback and locomotion, which are likely conveyed via different modulatory pathways.

Results

CT feedback modulates dLGN responses to naturalistic movie clips

To investigate the impact of CT feedback on naturalistic vision we showed head-fixed mice short movie clips, and compared responses of dLGN neurons during optogenetic suppression of V1 activity to a control condition with CT feedback left intact (**Fig. 1**). The responses of individual dLGN neurons to naturalistic movie clips were characterized by distinct response events that were narrow in time and reliable across trials (**Fig. 1d, top**, example neuron). Consistent with the notion that CT feedback has a modulatory rather than driving role [53], even during V1 suppression the temporal response pattern remained discernible (Pearson correlation $r = 0.54$, $p < 10^{-6}$, **Fig. 1d,e**). Yet, as illustrated in the example neuron, with CT feedback intact, firing rates were higher and burst spikes were less frequent (**Fig. 1e, left**). As a consequence, the distributions of instantaneous firing rates in the two conditions were significantly different (KS test, $p < 10^{-6}$), and were more skewed during V1 suppression than with CT feedback intact ($\gamma = 2.02$ vs. 1.22; **Fig. 1e, right**).

We observed similar effects in the recorded population of dLGN neurons, where CT feedback enhanced overall responses and promoted tonic mode firing. Indeed, while mean firing rates varied ~ 4 orders of magnitude across the population, they were higher with CT feedback intact than with feedback suppressed (13.6 vs. 10.9 spikes/s; linear multilevel-model (LMM): $F_{1,162.8} = 12.21$, $p = 0.00061$; **Fig. 1f**). In addition, CT feedback also influenced more fine-grained properties of geniculate responses. First, with CT feedback, the mean proportion of spikes occurring as part of a burst event was about half of what we observed during suppression (0.051 vs 0.093; LMM: $F_{1,172.8} = 44.3$, $p = 3.7 \times 10^{-10}$; **Fig. 1g**). Second, consistent with the distributions of firing rate for the example neuron (**Fig. 1e, right**) and related to the relative increase of responsiveness in the population (**Fig. S2c**), responses to the naturalistic movie clips with CT feedback intact were, on average, less sparse (0.37 vs. 0.46; LMM: $F_{1,169.21} = 51.89$, $p = 1.8 \times 10^{-11}$; **Fig. 1h**), indicating that neurons fired less selectively across the frames of the movie. Finally, we also examined the effect of CT feedback on response reliability. To quantify reliability, we computed the Pearson correlation coefficient of a neuron's responses between each pair of the 200 stimulus repeats per condition, and averaged the correlation coefficients over all pair-wise combinations [55]. With CT feedback intact, mean response reliability was lower than without feedback (0.17 vs. 0.19; LMM: $F_{1,169.73} = 15.2, p = 0.00014$; **Fig. 1i**). Importantly, this lower reliability did not show any systematic relation to the feedback modulation of firing rates (regression slope of -0.018 ± 0.19, estimated slope $\pm$ 2 $\times$ the estimated standard error, LMM, **Fig. 1j**). Taken together, these results indicate that CT feedback can modulate responses of dLGN neurons to naturalistic movie clips. The modulations are consistent with a net depolarizing effect, which supports higher firing rates and more linear, tonic firing mode, at the expense of sparseness and trial-to-trial reliability.

V1 suppression decreases dLGN responses to naturalistic movies by reducing response gain

To better understand the effects of V1 suppression on dLGN firing rate, we next asked whether the observed reduction in responsiveness could be explained by a divisive and/or subtractive mechanism (**Fig. 2**). Using repeated random sub-sampling cross-validation, we fit a simple threshold linear model (**Fig. 2a**, *inset*) to timepoint-by-timepoint responses in

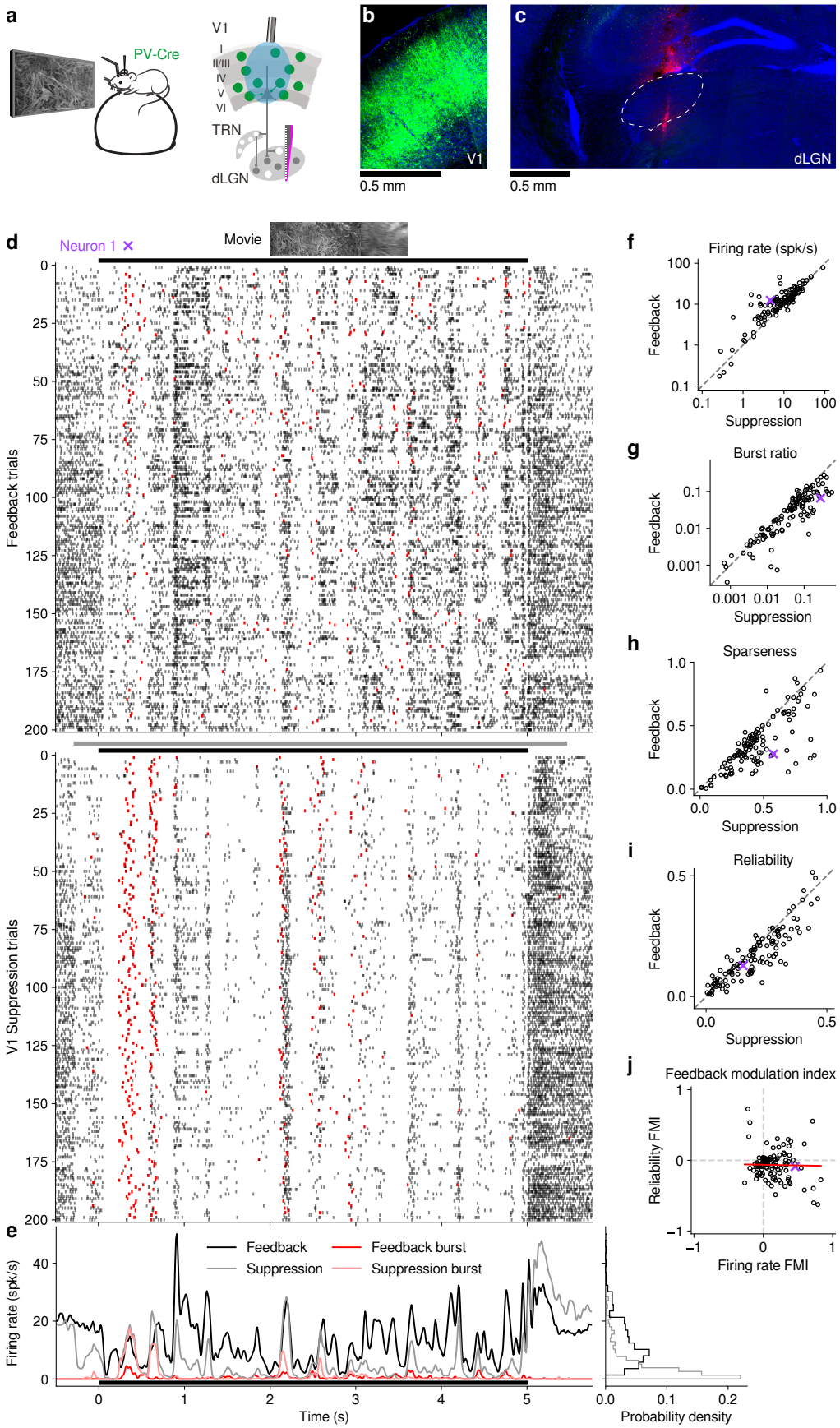

Figure 1 (**Previous page**) CT feedback modulates dLGN responses to wide-field naturalistic movie clips. (**a**) *Left*: Schematic of experimental setup. Head-fixed mice were placed on a floating Styrofoam ball and visual stimuli were presented on a screen located ∼25 cm away from the animal. *Right*: ChR2 was conditionally expressed in PV+ inhibitory interneurons (*green*) in all layers of V1 using a viral approach. Extracellular silicon electrode recordings were performed in dLGN with and without optogenetic suppression of V1. (**b**) Coronal section close to the V1 injection site for an example PV-Cre mouse (blue: DAPI; green: eYFP; Bregma: −3.4 mm). (**c**) Coronal section at the dLGN (white outline) recording site, same animal as in (b). For post-mortem confirmation of the electrode position, the back of the probe was stained with DiI (*magenta*) for one of the recording sessions (*blue*: DAPI; Bregma: −1.82 mm). (**d**) Raster plots of an example neuron for 200 presentations of a 5 s naturalistic movie clip, with CT feedback intact (control condition, *top*) and during V1 suppression (*bottom*). *Red*: burst spikes; *black bar*: movie clip presentation; *gray bar*: V1 suppression. (**e**) *Left*: PSTHs for both the feedback (*black*) and V1 suppression (*gray*) conditions. Superimposed are PSTHs of burst spikes only, separately for feedback (*red*) and suppression (*pale red*) conditions. *Right*: Corresponding instantaneous firing rate distributions. (**f–i**) Comparison of feedback vs. suppression conditions for mean firing rate (f), burst spike ratio (g), temporal sparseness (h), and response reliability (i), all calculated for the duration of the movie clip. For sample sizes, see **Table 1**. *Purple*: example neuron. Sparseness captures the activity fraction of a neuron, re-scaled between 0 and 1 [54]. Response reliability is defined as the mean Pearson correlation of all single trial PSTH pairs [55]. (**j**) Relation between CT feedback modulation of firing rate and reliability. Feedback effects were quantified with a feedback modulation index (FMI), where FMI = (feedback − suppressed)/(feedback + suppressed). See also **Fig. S2**.

suppression vs. feedback conditions, and extracted the slope and threshold of the fit for each subsample (**Fig. 2b,d**). In the two example neurons shown in **Fig. 2a-d**, the fitted slope was significantly smaller than 1 (neuron 2: median slope of 0.66, 95%–CI: 0.63–0.69, **Fig. 2b**; neuron 1: median slope of 0.37, 95%–CI: 0.32–0.41, **Fig. 2d**), while the threshold (x-intercept) was either small or not significantly different from 0 (neuron 2: median of 1.58, 95%–CI: 0.39–2.91; neuron 1: median of −0.14, 95%–CI: −1.49–0.89). We obtained similar results for the population of recorded neurons, where V1 suppression decreased the neurons' responses to naturalistic movie clips via a substantial change in gain (slope of 0.76 ± 0.1; LMM) without a significant shift in baseline (threshold of 0.013 ± 1.3; LMM; **Fig. 2e**). This demonstrates that V1 suppression influences responses in dLGN to naturalistic movie clips predominantly via a divisive mechanism.

We noticed that the threshold linear model could predict the effects of V1 suppression better for some neurons than for others. We therefore explored whether poor fits of the model might be related to our finding that V1 suppression can trigger non-linear, burst-mode firing. For instance, the threshold-linear model accurately captured the responses of example neuron 2 (median $R^2 = 0.90$, cross-validated; **Fig. 2a,b**), which exhibited little bursting during V1 suppression (burst ratio: 0.007). Neuron 1, in contrast, had a higher burst ratio during suppression (0.28) and the prediction (*blue*) sometimes overestimated or underestimated peaks in the actual response (*gray*), such that the percentage of explained variability was rather low (median $R^2 = 0.29$, cross-validated, **Fig. 2c,d**).

Indeed, across the population of recorded cells, the model goodness of fit (median R^2, cross-validated) during V1 suppression was inversely related to the burst ratio (slope of -1.4 ± 0.5; LMM; **Fig. 2f**), consistent with the notion that the highly non-linear, all-or-none-like burst mode firing [56] cannot be captured by the threshold-linear model. To further investigate the impact of bursting on response transformations by CT feedback, we re-computed the PSTHs for each neuron during V1 suppression after removing all burst spikes.

Removal of burst spikes allowed our model to capture the effects of V1 suppression even better (all spikes: mean $R^2 = 0.60$; non-burst spikes: mean $R^2 = 0.63$; LMM: $F_{1,150.49} = 7.6$, $p = 0.0066$; **Fig. 2g**). At the same time, removing burst spikes did not change our conclusion that the effect of CT feedback on movie responses was predominantly divisive (slope: 0.75 ± 0.09; threshold: 0.22 ± 1.33; LMM; **Fig. 2h**). Indeed, firing mode (all spikes vs. non-burst spikes) had no effect on either slope (LMM: $F_{1,153.7} = 0.57$, $p = 0.45$) or threshold estimates (LMM: $F_{1,150.64} = 0.21$, $p = 0.65$) of the simple linear model.

CT feedback modulates dLGN responses evoked by drifting gratings

Previous studies have investigated the effects of CT feedback using artificial stimuli, such as gratings and bars [25, 34, 41, 44]. To relate our findings to these studies, and to investigate the role of stimulus type, we next examined the effects of V1 suppression during the presentation of drifting gratings (**Fig. 3**). To approximate the visual stimulus configuration used for naturalistic movie clips, we presented full-field gratings drifting in one of 12 different orientations, and selected a pseudo-random subset of trials for V1 suppression. As expected, we found that responses of single dLGN neurons in the control condition with CT feedback intact could be modulated at the temporal frequency (TF, 4 cyc/s) of the drifting grating (**Fig. 3a$_1$, b$_1$**). Similar to previous studies in mouse dLGN [57–59], we also encountered some dLGN neurons with tuning for grating orientation or direction (**Fig. 3a$_2$, b$_2$**).

Remarkably, V1 suppression had mixed effects on dLGN responses to drifting gratings. Example neuron 1, for instance, had lower firing rates with CT feedback intact, both in the orientation tuning (**Fig. 3a$_2$**) and the cycle-averaged response to the preferred orientation (**Fig. 3a$_3$**). In addition, with CT feedback intact, there were markedly fewer burst spikes. In contrast, example neuron 3 responded more strongly with CT feedback intact (**Fig. 3b$_2$, b$_3$**). Such diverse effects of CT feedback were representative of the recorded population (**Fig. 3c**): V1 suppression during grating presentation reduced responses for some neurons, but increased responses for others, such that the average firing rates were almost identical (feedback: 14.3 spikes/s, suppression: 14.8 spikes/s) and statistically indistinguishable (LMM: $F_{1,67.8} = 0.17$, $p = 0.68$). In contrast to these diverse effects on firing rate, but similar to our findings for naturalistic movie clips, intact CT feedback was consistently associated with less bursting (burst ratios of 0.036 vs. 0.17; LMM: $F_{1,73.43} = 42.5$, $p = 7.7 \times 10^{-9}$; **Fig. 3d**).

Beyond studying overall changes in responsiveness and firing mode, we next asked how CT feedback affected the orientation selectivity of dLGN neurons. We computed orientation tuning curves separately for feedback and suppression conditions. For neuron 1, intact CT feedback was associated not only with lower average firing rates, but also poorer selectivity (OSIs of 0.14 vs. 0.25; **Fig. 3a$_2$**). In contrast, for neuron 3, orientation selectivity was similar during feedback and suppression conditions (OSIs of 0.1 vs. 0.09; **Fig. 3b$_2$**). These results were representative of the population, where CT feedback affected orientation selectivity in diverse ways, with virtually no difference in population means (feedback OSI: 0.14; suppression: 0.13; LMM: $F_{1,67} = 0.51$, $p = 0.48$; **Fig. 3e**; see also [25, 46, 47, 60]). For neurons with OSI > 0.02 and well-fit orientation tuning curves ($R^2 > 0.5$), preferred orientation during feedback and suppression conditions was largely similar, except for some cases where it shifted (**Fig. 3f**).

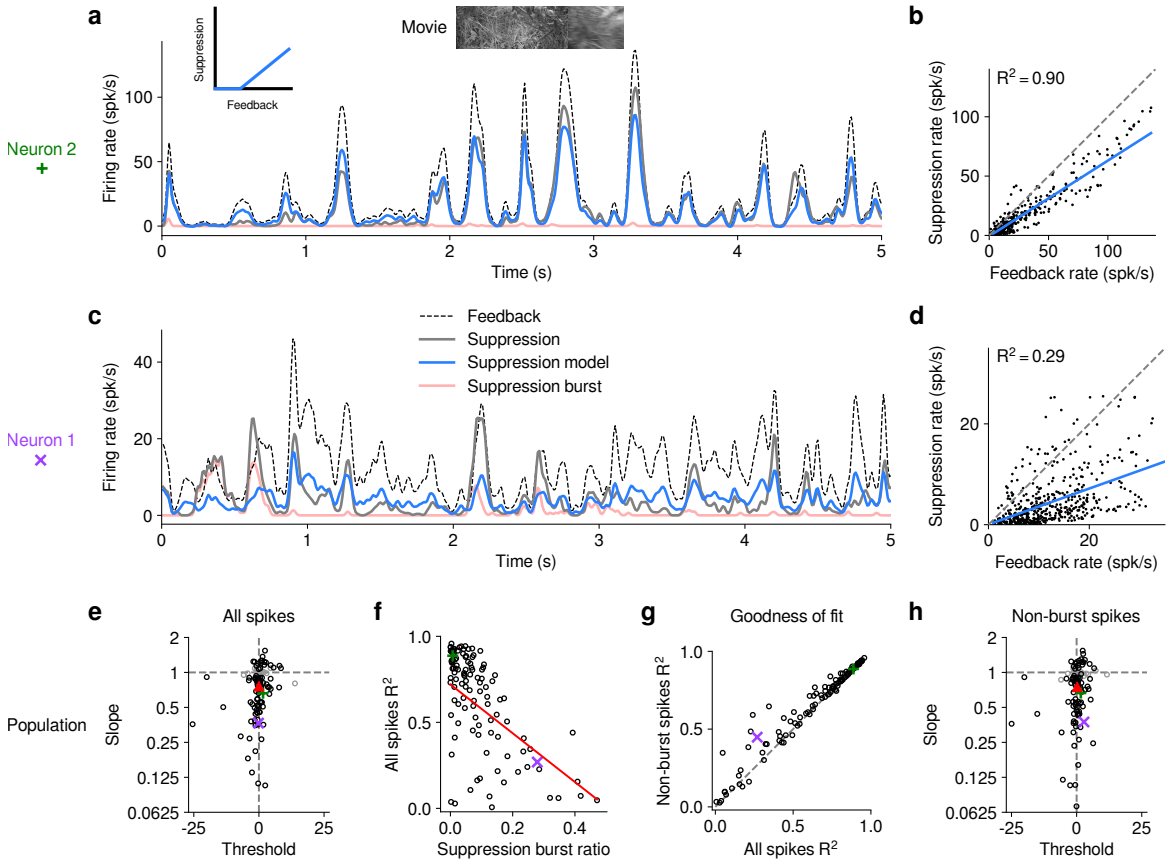

Figure 2 The effect of V1 suppression on dLGN responses to naturalistic movie clips is predominantly divisive.

(**a**) PSTHs of an example neuron during CT feedback (*black, dotted*) and V1 suppression (*gray*) conditions, for a random subset of 50% of trials per condition not used for model fitting. Responses during the suppression condition are approximated by the threshold linear model (*blue*) based on responses during the feedback condition. *Pale red:* PSTH during V1 suppression consisting only of burst spikes. *Inset*: cartoon of threshold linear model. (**b**) Timepoint-by-timepoint comparison of instantaneous firing rates of the PSTHs (derived from the 50% of trials not used for fitting) during the suppression vs. feedback conditions. PSTH data points are plotted at 0.01 ms resolution. *Blue line*: threshold linear model fit. (**c,d**) Same as (a,b) for a second example neuron (same as in **Fig. 1d,e**). (**e**) Slope and threshold parameters for all neurons. Each point represents the median for each neuron across 1000 random subsamples of trials. Black points indicate neurons with slopes significantly different from 1 (95%–CI). (**f**) Cross-validated model prediction quality (median R^2) vs. burst ratio during V1 suppression. *Red line*: LMM fit. (**g**) Model prediction quality with and without removal of burst spikes. (**h**) Same as (e) but with burst spikes removed. (e-h) *Purple, green*: example neurons; *red triangle*: LMM estimate of the mean.

Inspecting the spike rasters at different orientations, we realized that responses of geniculate neurons appeared to be more strongly modulated at the grating TF during V1 suppression than when feedback was intact (**Fig. 3a**$_1$). To test whether V1 suppression affected the ability of dLGN neurons to follow the gratings' temporal modulation, for each neuron we computed the amplitude of the response at the stimulus frequency (F_1 component) relative to the mean response (F_0 component) [61, 62] and found that F_1/F_0 ratios were indeed lower when feedback was intact (1.1 vs. 1.3; LMM: $F_{1,69} = 20.01$, $p = 3 \times 10^{-5}$; **Fig. 3g**). To explore the impact of CT feedback on the first harmonic response in more detail, we examined the cycle average responses to the preferred orientation, and asked how CT feedback affected response phase. Similar to the results obtained for the example neurons (**Fig. 3a**$_3$, **Fig. 3b**$_3$), we found that V1 suppression could advance response phase (**Fig. 3h**). This phase advance occurred more often for neurons whose responses during V1 suppression included a substantial proportion of burst spikes (**Fig. 3i**, *red*; 23 of 26 observations advanced, $p = 8.8 \times 10^{-5}$, binomial test) than for neurons whose V1 suppression responses had little or no bursting (**Fig. 3i**, *black*; 8 of 14 observations advanced, $p = 0.79$, binomial test), suggesting that the phase advance might be driven by the dynamics of burst spiking. In summary, these findings demonstrate that CT feedback can affect response phase, likely via its control of firing mode.

Effects of CT feedback on dLGN firing rates are more consistent for movies than gratings

Our analyses suggest that the impact of CT feedback on firing rates might be more consistent for naturalistic movie stimuli than for gratings. To test this hypothesis, we focused on the subset of neurons recorded with both types of stimuli. Indeed, when we compared feedback modulation indices (FMI) of firing rates, we found that for movies the overall FMI distribution was shifted towards more positive values (0.15 vs. 0.0046; LMM: $F_{1,35} = 13.66$, $p = 0.00075$; (**Fig. 4a**). This difference in FMI was not a consequence of the longer duration of V1 suppression during movie clips (**Fig. S3**). Remarkably, in 12/36 neurons (**Fig. 4a**, filled arrowheads) V1 suppression increased firing rates for gratings (negative grating FMI) [41] and decreased firing rates for movies (positive movie FMI), while the opposite effect only occurred in 1/36 neurons (open arrowhead). This sign change might be related to stimulus-dependent, feedback-mediated changes in bursting, which can drive high frequency firing. To test this hypothesis we compared CT feedback modulation of burst ratio for gratings vs. movie clips, and found that V1 suppression indeed induced stronger bursting for gratings than for movies (mean FMIs: -0.43 vs. -0.28; LMM: $F_{1,33} = 41.9$, $p = 2.4 \times 10^{-7}$; **Fig. 4b**). Thus, the stronger engagement of burst spiking for gratings might antagonize and overcome the reduction of firing rates that would otherwise occur during V1 suppression.

Effects of locomotion on dLGN responses resemble effects of CT feedback, but are independent

Previous studies have reported that responses of mouse dLGN neurons to grating stimuli are modulated by locomotion [63–65]. To assess how these findings extend to more complex stimuli, we separated the trials with CT feedback intact according to the animals' locomotion behavior. When we examined the spike rasters and PSTHs of example neuron 1 (**Fig. 5a,b**), we found that, despite preserved temporal features of the responses (Pearson correlation $r = 0.72$ between run and sit PSTHs, $p < 10^{-6}$), firing rates were higher overall during locomotion than stationary periods. Additionally, during locomotion, the distribution of firing rates was

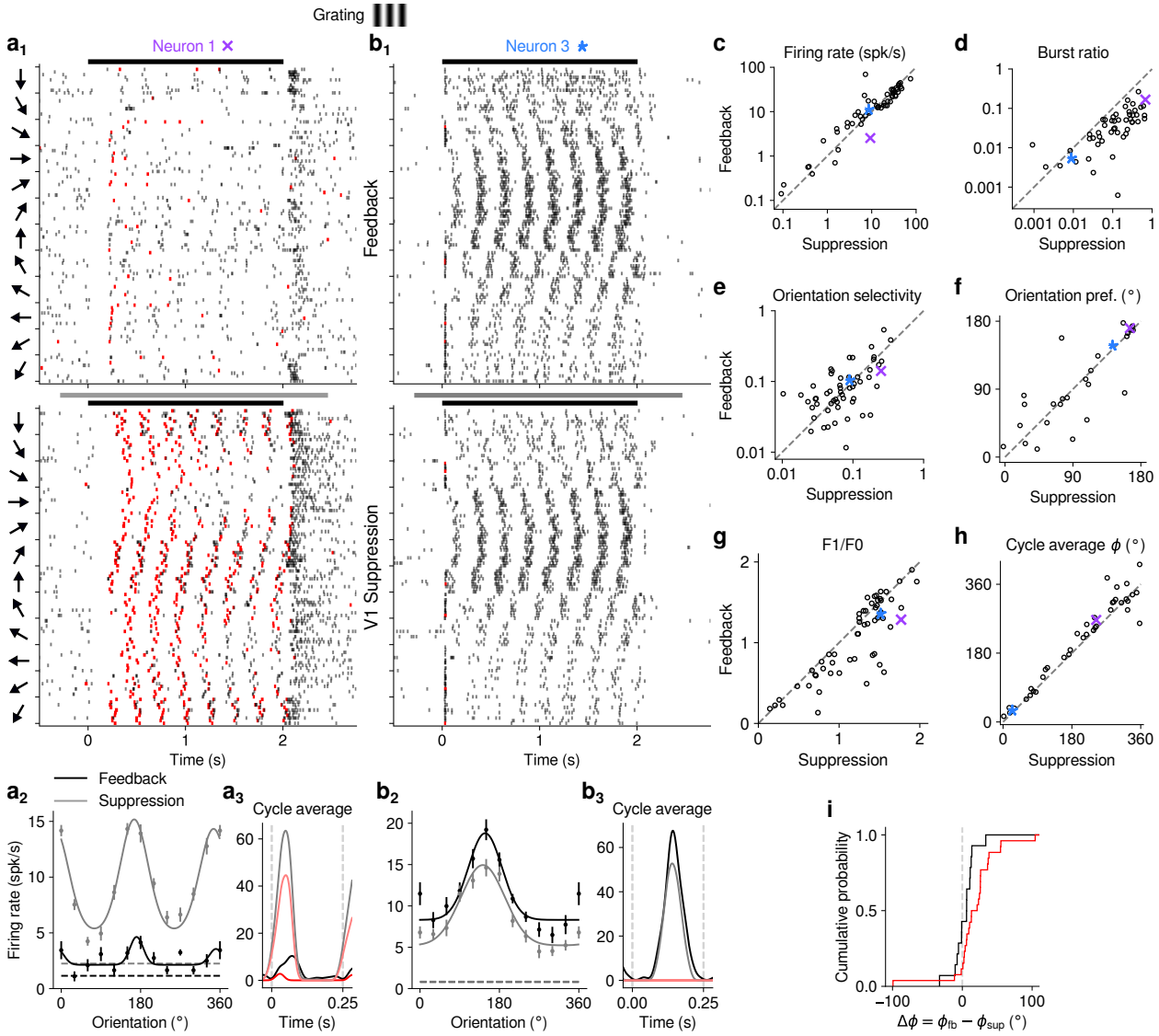

Figure 3 CT feedback modulates dLGN responses to drifting gratings.
(**a**) Responses of example neuron 1 (same as in **Fig. 1d,e** and **Fig. 2c,d**) to full-field, drifting gratings. (**a**$_1$) Raster plot in response to drifting gratings, with trials sorted by grating orientation (10 trials per orientation, 30° steps). *Red*: burst spikes. (**a**$_2$) Corresponding orientation tuning curve. Dashed lines represent spontaneous firing rates in response to medium gray screen. *Error bars*: standard error of the mean. (**a**$_3$) Cycle average response to preferred orientation. *Black, gray*: cycle average constructed from all spikes. *Red, pale red*: cycle average constructed from burst spikes only. *Black, red*: CT feedback intact; *gray, pale red*: V1 suppression. (**b**) Same as (a), for example neuron 3. (**c–h**) Comparison of conditions with CT feedback intact vs. V1 suppression, for mean firing rate (c), burst ratio (d), orientation selectivity index (OSI) (e), preferred orientation θ (f), F_1/F_0 (g), and cycle average phase ϕ (h). *Purple, blue*: example neurons. (**i**) Cumulative distribution of cycle average phase differences between feedback and suppression conditions. *Black*: neurons with little burst spiking (ratio of cycle average peak for burst spikes to cycle average peak for all spikes < 0.1); *red*: neurons with substantial burst spiking (ratio of cycle average peak for burst spikes to cycle average peak for all spikes ≥ 0.1).

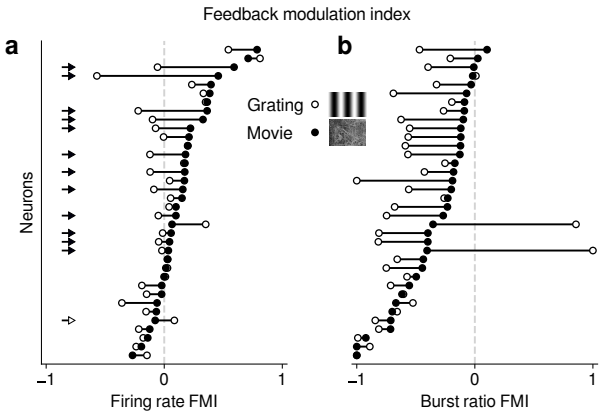

Figure 4 Effects of V1 suppression depend on stimulus type.
(**a,b**) Comparison of the strength of CT feedback effects (feedback modulation index, FMI), during processing of gratings and movie clips on (a) firing rates, and (b) burst ratio. Neurons are sorted along the ordinate according to their FMI in response to movies. *Black*: movie FMI; *white*: grating FMI. Arrows in (a) highlight neurons for which feedback modulation switches sign depending on stimulus type. For the statistical analysis in (b), we excluded the two outliers with highly positive FMIs for gratings, which showed no bursts or only one burst during V1 suppression. See also **Fig. S3**.

less skewed ($\gamma = 1.15$ vs. 1.45 during stationary trials), with a decrease in low and an increase in medium firing rates (KS test, $p < 10^{-6}$). A similar pattern was observed in the population of dLGN neurons, where firing rates were consistently higher for trials with locomotion compared to trials when the animal was stationary (13.31 vs. 10.27 spikes/s; LMM: $F_{1,193.2} = 15.5$, $p = 0.00012$; **Fig. 5c**). Similar to previous reports using gratings [63, 66], we found that bursting was lower during locomotion than stationary periods (0.046 vs. 0.071; LMM: $F_{1,186.7} = 28.9$, $p = 2.3 \times 10^{-7}$; **Fig. 5d**). Beyond these established measures, using movie clips allowed us to test the effects of locomotion on additional response properties: trials with locomotion were associated with lower sparseness (0.40 vs. 0.47; LMM: $F_{1,190.5} = 20.3$, $p = 1.2 \times 10^{-5}$; **Fig. 5e**) and lower response reliability (0.14 vs. 0.17; LMM: $F_{1,174.9} = 11.8$; $p = 0.00072$; **Fig. 5f**). This locomotion-related decrease of response reliability could be related to, but is likely not fully explained by, the increase in eye movements typically associated with running (**Fig. S4f,g**) [63, 67]. These analyses demonstrate that in dLGN, processing of naturalistic movie clips is robustly modulated by locomotion. Curiously, in all aspects tested, these modulations by locomotion had the same signatures as those of CT feedback: increased firing rates, reduced bursting, and decreased sparseness and reliability.

Since the effects of CT feedback and locomotion closely resembled each other, are the effects of locomotion on dLGN responses inherited via feedback from cortex? If so, neurons experiencing strong modulation by V1 suppression should also be strongly affected by locomotion (**Fig. 6a$_0$**). Contrary to this prediction, we found that effects of CT feedback (FMI) and behavioral state (run modulation index, RMI) were uncorrelated (firing rate: slope of 0.057 ± 0.13; burst ratio: slope of -0.11 ± 0.13; sparseness: slope of -0.061 ± 0.20; reliability: slope of -0.094 ± 0.12; **Fig. 6a$_{1-4}$**).

Moreover, if effects of locomotion on dLGN responses were inherited from primary visual cortex, such effects should vanish during V1 suppression (**Fig. 6b$_0$**). However, even during V1 suppression, RMIs were significantly different from 0 (firing rate: 0.17 ± 0.08; burst ratio:

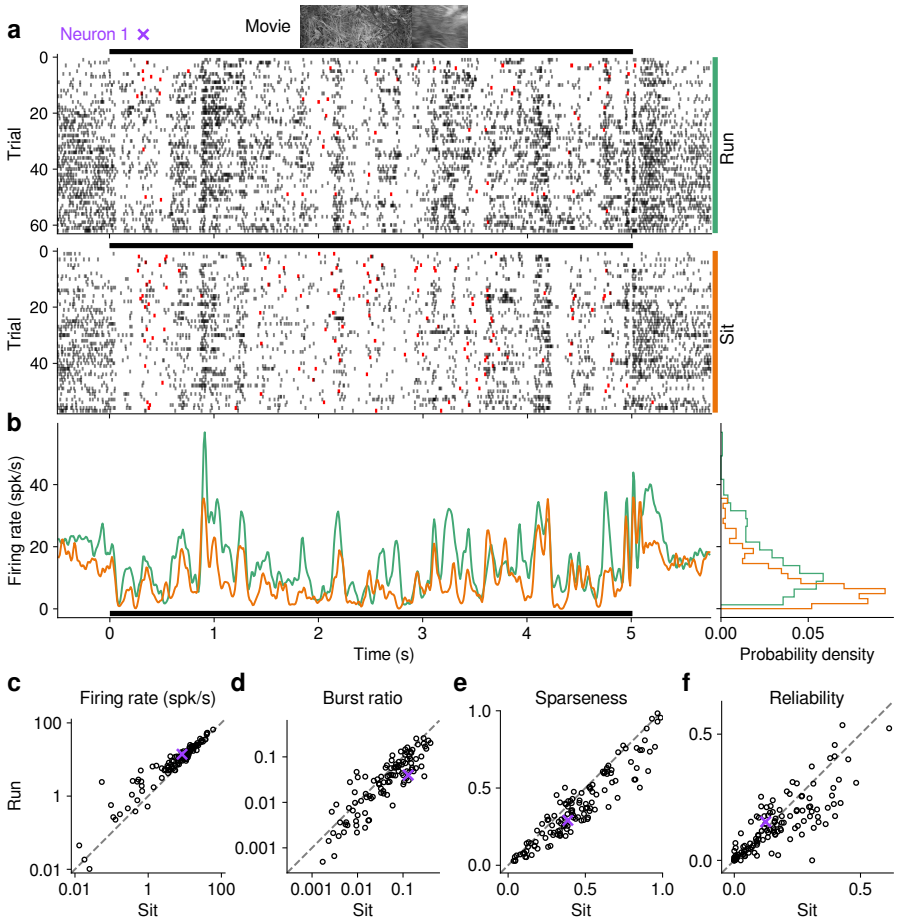

Figure 5 Effect of locomotion on dLGN responses are robust and resemble those of CT feedback.
(**a**) Spike raster of example neuron 1 (same as **Fig. 1d**) in response to a naturalistic movie clip during locomotion and stationary periods. *Top*: trials with run speed $>$ 1 cm/s; *bottom*: trials with run speed $<$ 0.25 cm/s, both for at least $>$ 50% of each trial. *Red*: burst spikes. (**b**) Corresponding PSTHs. *Green*: locomotion, *orange*: stationary; *black bar*: duration of movie clip. *Right*: Distribution of firing rates for run vs. sit trials. (**c–f**) Comparison of firing rates (c), burst ratio (d), sparseness (e), and reliability (f) during locomotion and stationary trials. See also **Fig. S4**.

-0.16 ± 0.14; sparseness: -0.12 ± 0.02; reliability: -0.11 ± 0.08; **Fig. 6b**$_{1-4}$). In fact, the degree of running modulation was correlated between feedback and suppression conditions (firing rate: slope of 0.48 ± 0.13; burst ratio: slope of 0.37 ± 0.21; sparseness: slope of 0.44 ± 0.14; reliability: slope of 0.50 ± 0.15; **Fig. 6b**$_{1-4}$). Interestingly, for firing rates and burst ratios, locomotion effects were slightly stronger, on average, with CT feedback intact compared to V1 suppression (RMI firing rate: 0.20 vs. 0.17; LMM: $F_{1,189.7} = 3.7$, $p = 0.055$, **Fig. 6b**$_1$; RMI burst ratio: -0.25 vs. -0.17; LMM: $F_{1,154.7} = 6.3$, $p = 0.013$, **Fig. 6b**$_2$), indicating that these two modulatory influences likely interact.

Lastly, we also tested the hypothesis that CT feedback might have a stronger impact during active behavioral states than during quiescence. If during quiescence feedback circuits were already completely disengaged, we should not have been able to observe further effects of V1 suppression (**Fig. 6c**$_0$). This was clearly not the case, because CT feedback effects were correlated across behavioral states (firing rate: slope of 0.72 ± 0.10; burst ratio: slope of 0.34 ± 0.15; sparseness: slope of 0.78 ± 0.12; reliability: slope of 0.43 ± 0.14; **Fig. 6c**$_{1-4}$). In addition, and similar to the slightly stronger RMIs during feedback, we discovered a locomotion-dependent feedback effect for firing rates and burst ratios. Feedback effects were slightly stronger, on average, during locomotion than during quiescence (FMI firing rate: 0.17 vs. 0.14; LMM: $F_{1,183.8} = 3.4$, $p = 0.067$; **Fig. 6c**$_1$; FMI burst ratio: -0.28 vs. -0.20; LMM: $F_{1,164.2} = 6.8$, $p = 0.010$; **Fig. 6c**$_2$). Our ability to observe effects of V1 suppression in dLGN while the animal was stationary suggests that CT feedback circuits are engaged even under conditions of behavioral quiescence and underscores that effects of CT feedback and behavioral state are largely independent. The more subtle interactions we observed between the two modulatory systems point towards a final common cellular or network effect, potentially related to depolarization levels of dLGN neurons.

Discussion

In this study we used naturalistic movies to reveal that corticothalamic feedback can have substantial and consistent effects on dLGN responses. First, we show that V1 suppression reduces time-varying dLGN firing rates, and leads to increases in bursting, sparseness and trial-to-trial reliability. While changes to time-varying firing rates were generally well predicted via a divisive reduction in response gain, a simple threshold-linear model could not capture the full spectrum of CT feedback effects, which include nonlinearities arising from burst spiking. Second, we demonstrate that behavioral state changes from locomotion to quiescence affect dLGN responses in a manner that closely resembles V1 suppression. We show, however, that the effects of V1 suppression on firing rate, bursting, sparseness and reliability are largely independent of modulations by behavioral state, and importantly, that effects of locomotion persist even when V1 activity is suppressed. Together, these findings demonstrate that behavioral modulations of dLGN activity are not simply inherited from cortex. Overall, our findings highlight the fact that dLGN activity can be reliably modulated by extra-retinal influences such as cortical feedback and locomotion, which exert their influences via largely separate routes.

To manipulate CT feedback, we chose a global V1 suppression approach based on optogenetic activation of ChR2 expressed in local PV+ inhibitory interneurons [41, 46–48, 68]. ChR2-based activation of local PV+ inhibitory interneurons is likely to result in reliable,

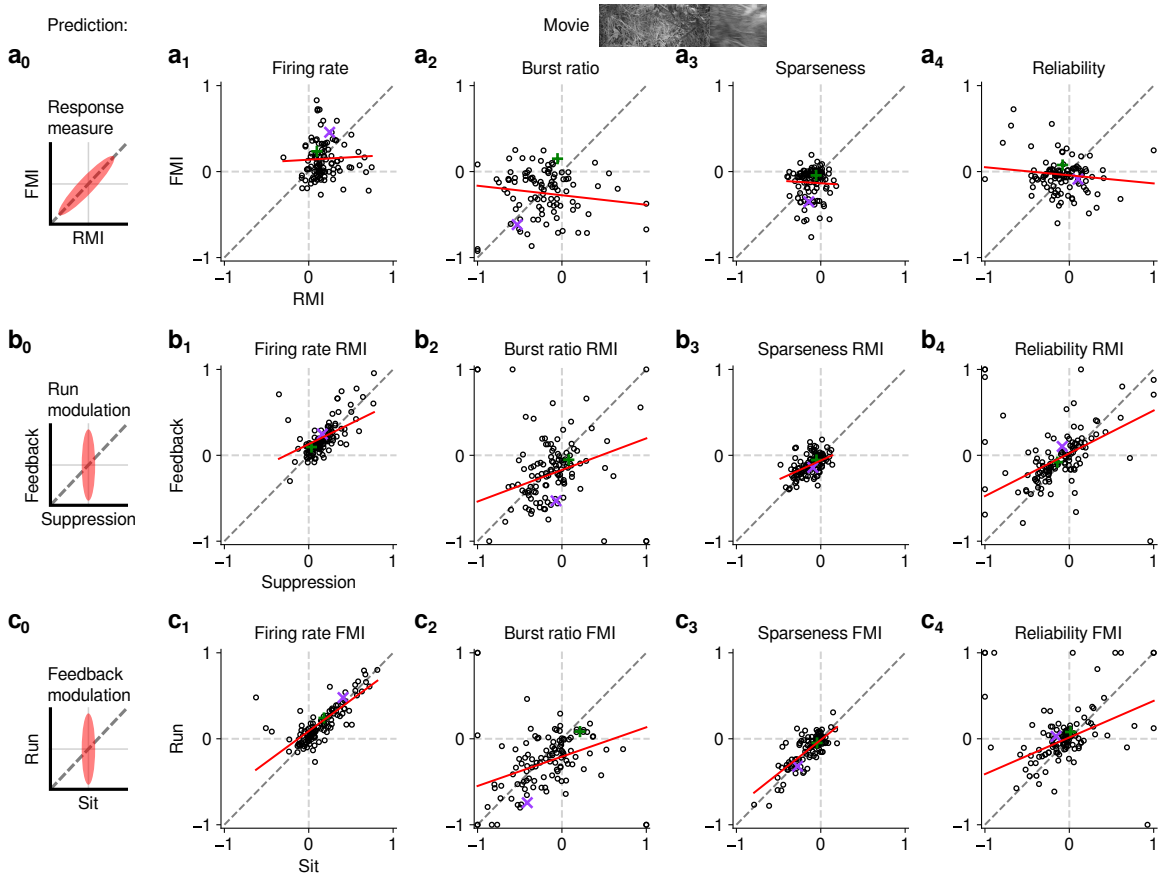

Figure 6 The effects of CT feedback and locomotion on movie responses were largely independent and similar in size.

($\mathbf{a}_0$–$\mathbf{c}_0$) Predicted relationships between modulation indices and response measures in different conditions, assuming dependence in the effects of CT feedback and locomotion. (**a**) Comparison of modulation by feedback (FMI) and modulation by running (RMI) for firing rates (a_1), burst ratio (a_2), sparseness (a_3), and reliability (a_4). Running effects were quantified with a run modulation index (RMI), where RMI = (running−sitting)/(running+sitting). (**b**) Comparison of modulation by running (RMI) during V1 suppression and CT feedback intact for firing rates (b_1), burst ratio (b_2), sparseness (b_3), and reliability (b_4). (**c**) Comparison of modulation by CT feedback (FMI) during locomotion and stationary periods for firing rates (c_1), burst ratio (c_2), sparseness (c_3), and reliability (c_4). *Red*: LMM fit. *Green, purple*: example neurons from **Fig. 2a,b**.

continuous, and strong suppression of V1 L6 CT neurons, compared to alternative optogenetic approaches involving direct photosuppression of L6 CT neurons. The latter approach involves the light-driven pumps archaerhodopsin and halorhodopsin [25, 41], and is challenging in terms of light power requirements, temporal decay of sensitivity, and effects on intracellular ion homeostasis [68, 69]. While silencing by excitation of inhibitory interneurons can exploit the robust effects of GABA-mediated inhibition in cortical circuits, it comes with a limitation in specificity. In addition to the direct L6 $\rightarrow$ thalamus circuit, indirect, polysynaptic effects might be exerted via alternative routes. One example is L5 corticofugal pyramidal cells projecting to the superior colliculus (SC), where tectogeniculate neurons in the superficial layers provide retinotopically organized, driving inputs to the dorsolateral shell region of the dLGN [70]. While global V1 suppression can indeed modulate the gain of SC responses [71, 72], direct optogenetic suppression of mouse SC evokes gain changes restricted to the most dorsal 150 μm of the dLGN [73]. The spatial spread of modulations we observed during V1 suppression clearly extended below the most dorsal electrode contacts, which is inconsistent with a major role of indirect SC contributions. To unequivocally rule out alternative routes, future studies are required that selectively suppress activity in V1 L6 CT neurons.

So far, studies using naturalistic stimuli to probe dLGN responses have been mostly performed in anesthetized animals and have not considered CT feedback [74–78]. Conversely, most studies investigating the impact of CT feedback have used artificial stimuli [25, 34, 41, 44]. Early experimental evidence already suggested that more complex visual patterns, and in particular moving stimuli, might better engage CT feedback circuits [17, 49]. From a conceptual perspective, if the role of feedback was to provide context based on an internal model built from the statistics of the world [79–82], natural stimuli would be expected to best comply with this model, and hence better drive these feedback mechanisms. Consistent with these ideas, we found that CT feedback-mediated modulations of firing rate were more consistent and therefore overall stronger for naturalistic movie clips than for gratings. A simple biophysical mechanism, however, might be sufficient to explain the differences of CT feedback effects for stimulus types: effects of V1 suppression on firing rate might have been masked for gratings, because their regular transitions from non-preferred to preferred phases strongly recruited high-frequency burst spiking. While movies have been little used in experimental studies of CT feedback, naturalistic input has recently been explored with a firing-rate based network model of the thalamo-cortico-thalamic circuit [83], which predicts that CT feedback during movie stimulation changes the autocorrelation of dLGN responses. Our results of increased sparseness during V1 suppression are grossly compatible with one model circuit architecture, which includes both short-delay inhibitory and long-delay excitatory feedback. Further analyses and an adaption of the model to properties of the mouse visual system would be required to draw firm conclusions.

In line with previous studies in non-human primates and cats [42–45], suppression of V1 activity revealed not only effects consistent with a robust role of CT feedback in enhancing the gain of geniculate responses, but also identified functional interactions with the neural mechanisms governing thalamic firing mode. Decreased responsiveness and a higher burst spike ratio during V1 suppression are consistent with a net hyperpolarization of dLGN neurons [56], which allows for the transient low-threshold calcium current (I_T) underlying thalamic bursting [84]. Indeed, intracellular recordings in cat dLGN revealed that cortical

ablation hyperpolarized the resting membrane potential by ∼9 mV, enough to push dLGN neurons into burst-firing mode [85]. Conversely, direct optogenetic activation of L6 CT neurons in primary somatosensory cortex has been shown to decrease burst mode firing [86]. Since firing rates are high during hyperpolarization-induced geniculate bursts [56], general decreases in response gain during V1 suppression could well be offset by burst firing. Indeed, during naturalistic movie stimulation, the threshold linear model systematically underestimated firing rates during bursting (**Fig. 2c,f–h**). Similarly, during grating stimulation, for which V1 suppression recruits burst firing more than for naturalistic movie stimulation (**Fig. 4b**), CT feedback did not have consistent effects on firing rate (**Fig. 3c**). Hyperpolarization of dLGN neurons and the resultant high frequency burst spiking, can, in principle, be achieved not only by a reduction of the direct excitatory influence of CT feedback, but also by an enhancement of its indirect, inhibitory impact [29]. Hence, diverse effects of CT feedback manipulation on firing rate are not surprising, in particular if firing mode is not taken into account. In the future, it will be important to characterize in detail the dependence of CT feedback effects on strength of suppression to get insights into the range of effects that CT feedback can exert.

Can the influence of feedback on dLGN firing mode allow us to assign a clear function to CT feedback? In burst firing mode, spontaneous activity is low, strongly rectified responses result in high signal-to-noise ratio [56], stimulus-evoked responses show phase-advance, and retinogeniculate [87] and cortical action potentials [88] are elicited with high efficiency. During processing of naturalistic stimuli, bursting can be triggered upon transition from non-preferred to preferred receptive field contents [75–77]. Such a response regime would be well suited for stimulus detection [56, 76, 89]. If stimulus detection were to then activate the CT feedback system, potentially in a spatially specific way, this could shift dLGN to tonic mode better suited for more linear, detailed image representation [56] (but see [90] for evidence from the somatosensory system that thalamic bursts might also carry information about stimulus detail). To understand if CT feedback is indeed recruited for detailed perceptual analyses, an essential next step would be to measure the activity of L6 CT neurons under behaviorally relevant conditions. Interestingly, in the auditory system, activation of L6 CT feedback has been shown to influence sound perception, with enhancements of sound detection or discrimination behavior, depending on the relative timing between CT spiking and stimulus onset [91].

By measuring the effects of V1 suppression during different behavioral states, we found that locomotion and CT feedback had similar effects on dLGN responses, but likely operated via separate circuits. The relationship between feedback and brain state has previously been investigated in the context of anesthesia, which can reduce the responsiveness of L6 CT neurons [31], and abolish activity in feedback projections from retrosplenial cortex to V1 [51]. One might therefore predict that CT feedback circuits might not be engaged during stationary periods compared to locomotion. In contrast to this prediction, we demonstrate here that cortical feedback modulated thalamic responses even during quiescence. While we found that V1 suppression lead to clear effects during stationary periods, we also revealed that CT feedback effects during locomotion were slightly stronger. This subtle interaction between brain state and feedback effects might relate to a previous finding, where careful dissection of brain states by depth of anesthesia had already suggested that the effects of transient cortical inactivation on dLGN responses were more evident during lighter anes-

thesia, i.e., during desynchronized cortical activity [43]. Thus, locomotion, light anesthesia and desynchronized brain states in general might leave more room for CT feedback to regulate membrane potential levels in dLGN, which in turn affects firing rates and bursting. Likewise, we found that effects of locomotion on dLGN responses [63–65] were clearly not inherited from cortex (see also [92]), but tended to be stronger when CT feedback was intact. Taken together, despite arising from independent sources, modulations by CT feedback and behavioral state had a similar phenotype and could interact in their modulation of dLGN activity. We speculate that this similarity points towards final shared cellular or network mechanisms, likely related to changes in the depolarization level of dLGN neurons.

Acknowledgments

This research was supported by DFG SFB870 TP19 (LB), DFG BU 1808/5-1 (LB), and by an add-on fellowship of the Joachim Herz Stiftung (GB). We thank D. Metzler for discussions regarding the multi-level modeling, M. Sotgia for lab management and support with animal handling and histology, S. Schörnich for IT support, and B. Grothe for providing excellent research infrastructure.

Author contributions

Conceptualization, L.B. and M.A.S; Methodology, M.A.S., D.C.; Software, M.A.S., S.K., G.B., D.C., L.B.; Formal Analysis, S.K.; Investigation, M.A.S.; Data Curation, M.A.S., G.B., D.C., L.B.; Writing – Original Draft, L.B., G.B.; Writing – Review & Editing, L.B., S.K., M.A.S., G.B., D.C.; Visualization, M.A.S., G.B., S.K.; Supervision, L.B.; Project Administration, L.B.; Funding Acquisition, L.B.

Declaration of Interests

The authors declare no competing interests.

Methods

All procedures complied with the European Communities Council Directive 2010/63/EC and the German Law for Protection of Animals, and were approved by local authorities, following appropriate ethics review.

Surgical procedures

Experiments were carried out in 6 adult PV-Cre mice (median age at first recording session: 24.71 weeks; B6;129P2-Pvalb$^{tm1(cre)Arbr}$/J; Jackson Laboratory) of either sex. Thirty minutes prior to the surgical procedure, mice were injected with an analgesic (Metamizole, 200 mg/kg, sc, MSD Animal Health, Brussels, Belgium). To induce anesthesia, animals were placed in an induction chamber and exposed to isoflurane (5% in oxygen, CP-Pharma, Burgdorf, Germany). After induction of anesthesia, mice were fixated in a stereotaxic frame (Drill & Microinjection Robot, Neurostar, Tuebingen, Germany) and the isoflurane level was lowered (0.5%–2% in oxygen), such that a stable level of anesthesia could be achieved

as judged by the absence of a pedal reflex. Throughout the procedure, the eyes were covered with an eye ointment (Bepanthen, Bayer, Leverkusen, Germany) and a closed loop temperature control system (ATC 1000, WPI Germany, Berlin, Germany) ensured that the animal's body temperature was maintained at 37° C. At the beginning of the surgical procedure, an additional analgesic was administered (Buprenorphine, 0.1 mg/kg, sc, Bayer, Leverkusen, Germany) and the animal's head was shaved and thoroughly disinfected using idodine solution (Braun, Melsungen, Germany). Before performing a scalp incision along the midline, a local analgesic was delivered (Lidocaine hydrochloride, sc, bela-pharm, Vechta, Germany). The skin covering the skull was partially removed and cleaned from tissue residues with a drop of H_2O_2 (3%, AppliChem, Darmstadt, Germany). Using four reference points (bregma, lambda, and two points 2 mm to the left and to the right of the midline respectively), the animal's head was positioned into a skull-flat configuration. The exposed skull was covered with OptiBond FL primer and adhesive (Kerr dental, Rastatt, Germany) omitting three locations: V1 (AP: -2.8 mm, ML: -2.5 mm), dLGN (AP: -2.3 mm, ML: -2 mm), and a position roughly 1.5 mm anterior and 1 mm to the right of bregma, designated for a miniature reference screw (00-96 X 1/16 stainless steel screws, Bilaney) soldered to a custom-made connector pin. 2 μL of the adeno-associated viral vector rAAV9/1.EF1a.DIO.hChR2(H134R)-eYFP.WPRE.hGH (Addgene, #20298-AAV9) was dyed with 0.3 μL fast green (Sigma-Aldrich, St. Louis, USA). After performing a small craniotomy over V1, a total of $\sim$0.5 μL of this mixture was injected across the entire depth of cortex (0.05 μL injected every 100 μm, starting at 1000 μm and ending at 100 μm below the brain surface), using a glass pipette mounted on a Hamilton syringe (SYR 10 μL 1701 RN no NDL, Hamilton, Bonaduz, Switzerland). A custom-made lightweight stainless steel head bar was positioned over the posterior part of the skull such that the round opening contained in the bar was centered on V1/dLGN and attached with dental cement (Ivoclar Vivadent, Ellwangen, Germany) to the primer/adhesive. The opening was later filled with the silicone elastomer sealant Kwik-Cast (WPI Germany, Berlin, Germany). At the end of the procedure, an antibiotic ointment (Imax, Merz Pharmaceuticals, Frankfurt, Germany) was applied to the edges of the wound and a long-term analgesic (Meloxicam, 2 mg/kg, sc, Böhringer Ingelheim, Ingelheim, Germany) was administered and continued to be administered for 3 consecutive days. For at least 5 days post-surgery, the animal's health status was assessed via a score sheet. After at least 1 week of recovery, animals were gradually habituated to the experimental setup by first handling them and then simulating the experimental procedure. To allow for virus expression, neural recordings started no sooner than 3 weeks after injection. On the day prior to the first day of recording, mice were fully anesthetized using the same procedures as described for the initial surgery, and a craniotomy (ca. 1.5 mm^2) was performed over dLGN and V1 and re-sealed with Kwik-Cast (WPI Germany, Berlin, Germany). As long as the animals did not show signs of discomfort, the long-term analgesic Metacam was administered only once at the end of surgery, to avoid any confounding effect on experimental results. Recordings were performed daily and continued for as long as the quality of the electrophysiological signals remained high.

Electrophysiological recordings, optogenetic suppression of V1, perfusion

Head-fixed mice were placed on an air-cushioned Styrofoam ball, which allowed the animal to freely move. Two optical computer mice interfaced with a microcontroller (Arduino

Duemilanove) sampled ball movements at 90 Hz. To record eye position and pupil size, the animal's eye was illuminated with infrared light and monitored using a zoom lens (Navitar Zoom 6000) coupled with a camera (Guppy AVT camera; frame rate 50 Hz, Allied Vision, Exton, USA). Extracellular signals were recorded at 30 kHz (Blackrock microsystems). For each recording session, the silicon plug sealing the craniotomy was removed. For V1 recordings, a 32 or 64 channel silicon probe (Neuronexus, A1x32-5mm-25-177 or A1x64-Poly2-6mm-23s-160) was lowered into the brain to a median depth of 1100 μm. For dLGN recordings, a 32 channel linear silicon probe (Neuronexus A1x32Edge-5mm-20-177-A32, Ann Arbor, USA) was lowered to a depth of ∼2700–3700 μm below the brain surface. We judged recording sites to be located in dLGN based on the characteristic progression of RFs from upper to lower visual field along the electrode shank [57] (**Fig. S1b**), the presence of responses strongly modulated at the temporal frequency of the drifting gratings (F1 response), and the preference of responses to high temporal frequencies [57, 93]. For *post hoc* histological reconstruction of the recording site, the electrode was stained with DiI (Invitrogen, Carlsbad, USA) for one of the final recording sessions.

For photostimulation of V1 PV+ inhibitory interneurons, an optic fiber (910 μm diameter, Thorlabs, Newton, USA) was coupled to a light-emitting diode (LED, center wavelength 470 nm, M470F1, Thorlabs, Newton, USA) and positioned with a micromanipulator less than 1 mm above the exposed surface of V1. A black metal foil surrounding the tip of the head bar holder prevented the photostimulation light from reaching the animal's eyes. To ensure that the photostimulation was effective, the first recording session for each mouse was carried out in V1. Only if the exposure to light reliably induced suppression of V1 activity was the animal used for subsequent dLGN recordings. For both movie clips and drifting gratings, photostimulation started 0.25 s before stimulus onset and ended 0.5 s after stimulus offset. LED light intensity was adjusted on a daily basis to evoke reliable effects (median intensity: 27.5 mW/cm^2) as measured at the tip of the optic fiber. Since the tip of the fiber never directly touched the surface of the brain, and since the clarity of the surface of the brain varied (generally decreasing every day following the craniotomy), the light intensity delivered even to superficial layers of V1 was inevitably lower. Importantly, changes in dLGN firing rates induced by V1 suppression (FMI, see below) did not differ, on average, from those induced by behavioral state (RMI, see below) (firing rate: FMI 0.20 vs. RMI 0.15, LMM: $F_{1,145.7} = 3.02$, $p = 0.08$; burst ratio: FMI −0.27 vs. RMI −0.28, $F_{1,124.0} = 0.002$, $p = 0.97$; sparseness: FMI −0.12 vs. RMI −0.14, $F_{1,144.9} = 1.03$, $p = 0.31$; reliability: FMI −0.084 vs. −0.037, $F_{1,183.0} = 1.96$, $p = 0.16$; **Fig. 6a**), indicating that optogenetic stimulation effects were not outside the physiological range.

After the final recording session, mice were first administered an analgesic (Metamizole, 200 mg/kg, sc, MSD Animal Health, Brussels, Belgium) and following a 30 min latency period were transcardially perfused under deep anesthesia using a cocktail of Medetomidin (0.5 ml/kg) Midazolam (1 ml/kg) and Fentanyl (1 ml/kg) (ip). Perfusion was first done with Ringer's lactate solution followed by 4% paraformaldehyde (PFA) in 0.2 M sodium phosphate buffer (PBS).

Histology

To verify recording site and virus expression, we performed histological analyses. Brains were removed, postfixed in PFA for 24 h, and then rinsed with and stored in PBS at 4°

C. Slices (40 μm) were cut using a vibrotome (Leica VT1200 S, Leica, Wetzlar, Germany), mounted on glass slides with Vectashield DAPI (Vector Laboratories, Burlingame, USA), and coverslipped. A fluorescent microscope (BX61 Systems Microscope, Olympus, Tokyo, Japan) was used to inspect slices for the presence of yellow fluorescent protein (eYFP) and DiI. Recorded images were processed using FIJI [94, 95].

Visual stimulation

Visual stimuli were presented on a liquid crystal display (LCD) monitor (Samsung SyncMaster 2233RZ; mean luminance 50 cd/m^2, 60 Hz) positioned at 25 cm distance from the animal's right eye using custom written software (EXPO, https://sites.google.com/a/nyu.edu/expo/home). The display was gamma-corrected for the presentation of artificial stimuli, but not for movies (see below).

To measure receptive fields (RFs), we mapped the ON and OFF subfields with a sparse noise stimulus. The stimulus consisted of nonoverlapping white and black squares on a square grid, each flashed for 200 ms. For dLGN recordings, the square grid spanned 60° on a side, while individual squares spanned 5° on a side. For subsequent choices of stimuli, RF positions and other tuning preferences were determined online after each experiment based on multiunit activity, i.e. high-pass filtered signals crossing a threshold of 4.5 to 6.5 SD.

We measured single unit orientation preference by presenting full-field, full-contrast drifting sinusoidal gratings of 12 different, pseudo-randomly interleaved orientations (30° steps). For dLGN recordings, spatial frequency was either 0.02 cyc/° (3 experiments) or 0.04 cyc/° (8 experiments) and temporal frequency was either 2 Hz (2 experiments) or 4 Hz (9 experiments). One blank condition (i.e., mean luminance gray screen) was included to allow measurements of baseline activity. The stimulus duration was 2 s, with an interstimulus interval (ISI) of 2.4 s.

For laminar localization of neurons recorded in V1, we presented a full-field, contrast-reversing checkerboard at 100% contrast, with a spatial frequency of either 0.01 cyc/° (2 experiments) or 0.02 cyc/° (5 experiments) and a temporal frequency of 0.5 cyc/s.

Movies were acquired using a hand-held consumer-grade digital camera (Canon PowerShot SD200) at a resolution of 320×240 pixels and 60 frames/s. Movies were filmed close to the ground in a variety of wooded or grassy locations in Vancouver, BC, and contained little to no forward/backward optic flow, but did contain simulated gaze shifts (up to 275°/s), generated by manual camera movements (for example movies, see **Fig. S5**). Focus was kept within 2 m and exposure settings were set to automatic. The horizontal angle subtended by the camera lens was 51.6°. No display gamma correction was used while presenting movies, since consumer-grade digital cameras are already gamma corrected for consumer displays [96]. For presentation, movies were cut into 5 s clips and converted from color to grayscale. Movie clips were presented with an ISI of 1.25 s (32 experiments).

Spike sorting

To obtain single unit activity from extracellular recordings, we used the open source, Matlab-based, automated spike sorting toolbox Kilosort [97]. Resulting clusters were manually refined using Spyke [98], a Python application that allows the selection of channels and time ranges around clustered spikes for realignment, as well as representation in 3D

space using dimension reduction (multichannel PCA, ICA, and/or spike time). In 3D, clusters were then further split via a gradient-ascent based clustering algorithm (GAC) [99]. Exhaustive pairwise comparisons of similar clusters allowed the merger of potentially over-clustered units. For subsequent analyses, we inspected autocorrelograms and mean voltage traces, and only considered units that displayed a clear refractory period and a distinct spike waveshape. All further analyses were carried out using the DataJoint framework [100] with custom-written code in Python.

Response characterization

We used current source density (CSD) analysis for recordings in area V1 to determine the laminar position of electrode contacts. To obtain the LFP data we first down-sampled the signal to 1 kHz before applying a bandpass filter (4–90 Hz, 2^{nd}-order Butterworth filter). We computed the CSD from the second spatial derivative of the local field potentials [101], and assigned the base of layer 4 to the contact that was closest to the earliest CSD polarity inversion. The remaining contacts were assigned to supragranular, granular and infragranular layers, assuming a thickness of $\sim$1 mm for mouse visual cortex [102].

In recordings targeting dLGN, we used the envelope of multi-unit spiking activity (MUAe) [103] to determine RF progression (**Fig. S1b**). Briefly, we full-wave rectified the high-pass filtered signals (cutoff frequency: 300 Hz, 4^{th}-order non-causal Butterworth filter) before performing common average referencing by subtracting the median voltage across all channels in order to eliminate potential artifacts (e.g. movement artifacts). We then applied a low-pass filter (cutoff frequency: 500 Hz, Butterworth filter) and down-sampled the signal to 2 kHz. Recording sessions for which RFs did not show the retinotopic progression typical of dLGN (**Fig. S1b**) [57] were excluded from further analysis.

Each unit's peristimulus time histogram (PSTH, i.e., the response averaged over trials) was calculated by convolving a Gaussian of width $2\sigma = 20$ ms with the spike train collapsed across all trials, separately for each condition.

We defined bursts according to [44], which required a silent period of at least 100 ms before the first spike in a burst, followed by a second spike with an interspike interval < 4 ms. Any subsequent spikes with preceding interspike intervals < 4 ms were also considered to be part of the burst. All other spikes were regarded as tonic. We computed a burst ratio (the number of burst spikes divided by the total number of spikes) and compared this ratio in conditions with CT feedback intact vs. V1 suppression or during locomotion vs. stationary conditions. PSTHs for burst spikes were calculated by only considering spikes that were part of bursts before collapsing across trials and convolving with the Gaussian kernel (see above). PSTHs for non-burst spikes were calculated in an analogous way.

To quantify the effect of V1 suppression on various response properties, we defined the feedback modulation index (FMI) as

$$\text{FMI} = \frac{\text{feedback} - \text{suppression}}{\text{feedback} + \text{suppression}} \tag{1}$$

Characterization of responses to naturalistic movie clips

Signal to noise ratio (SNR) was calculated according to [104] by

$$\mathrm{SNR} = \frac{Var[\langle C_r \rangle]_t}{\langle Var[C]_t \rangle_r} \tag{2}$$

where C is the T by R response matrix (time samples by stimulus repetitions) and $\langle\rangle_x$ and $\mathrm{Var}[]_x$ denote the mean and variance across the indicated dimension, respectively. If all trials were identical such that the mean response was a perfect representative of the response, SNR would equal 1.

The sparseness S of a PSTH was calculated according to [54] by

$$S = \left(1 - \frac{\left(\sum_{i=1}^{n} r_i/n\right)^2}{\sum_{i=1}^{n} r_i^2/n}\right)\left(\frac{1}{1-1/n}\right) \tag{3}$$

where $r_i \geq 0$ is the signal value in the i^{th} time bin, and n is the number of time bins. Sparseness ranges from 0 to 1, with 0 corresponding to a uniform signal, and 1 corresponding to a signal with all of its energy in a single time bin.

Response reliability was quantified according to [55] as the mean pairwise correlation of all trial pairs of a unit's single trial responses. Single trial responses were computed by counting spikes in 20 ms, overlapping time bins at 1 ms resolution. Pearson's correlation was calculated between all possible pairs of trials, and then averaged across trials per condition.

To detect response peaks in trial raster plots and measure their widths, clustering of spike times collapsed across trials was performed using the gradient ascent clustering (GAC) algorithm [99], with a characteristic neighborhood size of 20 ms. Spike time clusters containing less than 5 spikes were discarded. The center of each detected cluster of spike times was matched to the nearest peak in the PSTH. A threshold of $\theta = b + 3$ Hz was applied to the matching PSTH peak, where $b = 2\,\mathrm{median}(x)$ is the baseline of each PSTH x. Peaks in the PSTH that fell below θ were discarded, and all others were kept as valid peaks. Peak widths were measured as the temporal separation of the middle 68% (16th to 84th percentile) of spike times within each cluster.

To determine whether V1 suppression changes dLGN responses in a divisive or subtractive manner, we fit a threshold-linear model using repeated random subsampling cross-validation. To this end, we first selected a random set of 50% of the trials for each condition for fitting to the timepoint-by-timepoint responses a threshold linear model given by $r_{supp} = s\, r_{fb} + b$, where $r_{supp} > 0$, with s representing the slope and b the offset. Fitting was done using non-linear least squares (`scipy.optimize.curve_fit`). Throughout **Fig. 2**, we report the resulting x-intercept as the threshold. We evaluated goodness of fit (R^2) for the other 50% of trials not used for fitting. We repeated this procedure 1000 times and considered threshold and slope as significant if the central 95% of their distribution did not include 0 and 1, respectively.

Characterization of responses to drifting gratings

For display of spike rasters (**Fig. 3**), trials were sorted by condition. We computed orientation tuning curves by fitting a sum of two Gaussians of the same width with peaks 180° apart:

$$R(\theta) = R_0 + R_p e^{-\frac{(\theta-\theta_p)^2}{2\sigma^2}} + R_n e^{-\frac{(\theta-\theta_p+180)^2}{2\sigma^2}} \tag{4}$$

In this expression, θ is stimulus orientation (0–360°). The function has five parameters: preferred orientation θ_p, tuning width σ, baseline response R_0, response at the preferred orientation R_p, and response at the null orientation R_n.

Orientation selectivity was quantified according to [41, 105] as

$$\text{OSI} = \frac{\sqrt{(\sum r_k \sin(2\theta_k))^2 + (\sum r_k \cos(2\theta_k))^2}}{\sum r_k} \tag{5}$$

where r_k is the response to the kth direction given by θ_k. We determined OSI for each unit during both feedback and suppression conditions.

We computed the first harmonic of the response r from the spike trains according to [62] to obtain the amplitude and phase of the best-fitting sinusoid, which has the same temporal frequency as the stimulus. For each trial, we calculated

$$r = (1/D) \sum_k \cos(2\pi f t_k) + i \sin(2\pi f t_k) \tag{6}$$

where D is the stimulus duration, f is the temporal frequency of the stimulus, and the t_k are the times of the individual spikes. We excluded the first cycle to avoid contamination by the onset response. For (**Fig. 3g**), we calculated average amplitude F_1 by obtaining the absolute value of the complex number r on each trial, before averaging across trials, to avoid potential confounds due to differences in response phase across conditions. For the comparison of response phase, we focused on the orientation which elicited the maximal cycle average response across both feedback and suppression conditions.

Exclusion criteria

Neurons with mean evoked firing rates < 0.01 spikes/s were excluded from further analysis. For movie clips, only neurons with SNR ≥ 0.015 in at least one of the conditions in an experiment were considered. Of this population, 2 neurons were excluded from the analysis of the parameters returned by the threshold linear model, because their R^2 was < 0. For gratings, we converted firing rates in response to each orientation to z-scores relative to responses to the mean luminance gray screen. We only considered visually responsive neurons, which had a z-scored response ≥ 2.5 to at least 1 orientation. For the analysis of response phase, we only considered neurons with a peak of the cycle average response of at least 10 Hz in both feedback and suppression conditions, and an F_1/F_0 ratio of at least 0.25.

Locomotion

We used the Euclidean norm of three perpendicular components of ball velocity (roll, pitch and yaw) to compute animal running speed. For the analysis of neural responses as a function of behavioral state, locomotion trials were defined as those for which speed exceeded

1 cm/s for at least 50% of the stimulus presentation, and stationary trials as those for which speed fell below 0.25 cm/s for at least 50% of the stimulus presentation. To quantify the effect of running vs. sitting on various response properties, the run modulation index (RMI) was defined as

$$\mathrm{RMI} = \frac{\mathrm{running} - \mathrm{sitting}}{\mathrm{running} + \mathrm{sitting}} \tag{7}$$

Eye Tracking

The stimulus viewing eye was filmed using an infrared camera under infrared LED illumination. Pupil position was extracted from the videos using a custom, semi-automated algorithm. Briefly, each video frame was equalized using an adaptive bi-histogram equalization procedure, and then smoothed using a median and bilateral filters. The center of the pupil was detected by taking the darkest point in a convolution of the filtered image with a black square. Next, the peaks of the image gradient along lines extending radially from the center point were used to define the pupil contour. Lastly, an ellipse was fit to the contour, and the center of this ellipse was taken as the position of the pupil. A similar procedure was used to extract the position of the corneal reflection (CR) of the LED illumination. Eye blinks were automatically detected and the immediately adjacent data points were excluded. Adjustable algorithm parameters were set manually for each experiment. Output pupil position time-courses were lightly smoothed, and unreliable segments were automatically removed according to *a priori* criteria. Finally, the CR position was subtracted from the pupil position to eliminate translational eye movements, and pupil displacement in degrees relative to the baseline (median) position was determined by

$$\theta = 2\,\frac{\arcsin(d/2)}{r} \tag{8}$$

where d is the distance between the pupil and the baseline position, and $r = 1.25$ mm is the radius of the eye [106]. Angular displacement was computed separately for x and y directions and then combined geometrically to give the final measure of distance from baseline.

Statistical methods

To assess statistical significance, we fitted and examined multilevel linear models [107]. Such models take into account the hierarchical structure present in our data (i.e., neurons nested in experiments, experiments nested in recording sessions, recordings sessions nested in animals), and eliminate the detrimental effect of structural dependencies on the likelihood of Type I errors (false positive reports) [108]. By considering the nested structure of the data, multilevel models also eliminate the need for "pre-selecting" data sets, such as one out of several experiments repeatedly performed on the same neurons. Whenever we have several experiments per neuron, we include all of them, and also show them in the scatter plots ("observations"). We provide the sample size for each analysis in **Table 1**. In fitting the models, we accounted for repeated measures by including random effects for animals, recording sessions, experiments, and neurons. We fit these models in R [109], using the *lme4* package [110]. We estimated F-values, their degrees of freedom, and the corresponding p-values using the Satterthwaite approximation [111] implemented by the *lmertest* package

[112]. Throughout, uncertainty in estimated regression slopes is represented as $slope \pm x$, where x is 2 $\times$ the estimated standard error of the slope.

	Observations	**Neurons**	**Mice**
Figure 1f	118	64	6
Figure 1g	117	63	6
Figure 1h–j	118	64	6
Figure 2e,h	114	62	6
Figure 2f	113	61	6
Figure 2g	113	62	6
Figure 3c–e	57	44	4
Figure 3f	27	26	4
Figure 3g	57	44	4
Figure 3h,i	40	33	3
Figure 4a	36	36	3
Figure 4b	34	34	3
Figure 5c,e	129	65	6
Figure 5d	124	63	6
Figure 5f	128	65	6
Figure $6a_1$,a_3,a_4	109	59	6
Figure $6a_2$	101	56	6
Figure $6b_1$,b_3	126	64	6
Figure $6b_2$	109	58	6
Figure $6b_4$	111	63	6
Figure $6c_1$,c_3	123	63	6
Figure $6c_2$	110	58	6
Figure $6c_4$	109	62	6
Figure S2a,c,e	118	64	6
Figure S2b,f	108	57	6
Figure S2d	117	63	6
Figure S3a,b	118	64	6
Figure S3c,d	39	39	4
Figure S4a,d	129	65	6
Figure S4b	102	56	6
Figure S4c	107	57	6
Figure S4e,g	125	65	6

Table 1 Breakdown of sample sizes (N) for the analyses of neural data. See text for details.

References

1. Lien, A.D. and Scanziani, M. (2018). Cortical direction selectivity emerges at convergence of thalamic synapses. Nature *558*, 80–86.

2. Hubel, D.H. and Wiesel, T.N. (1962). Receptive fields, binocular interaction and functional architecture in the cat's visual cortex. Journal of Physiology *160*, 106–154.

3. Chance, F.S., Nelson, S.B., and Abbott, L.F. (1999). Complex cells as cortically amplified simple cells. Nat Neurosci *2*, 277–282.

4. Riesenhuber, M. and Poggio, T. (1999). Hierarchical models of object recognition in cortex. Nature Neuroscience *2*, 1019.

5. Riesenhuber, M. and Poggio, T. (2000). Models of object recognition. Nature Neuroscience *3*, 1199–1204.

6. DiCarlo, J.J., Zoccolan, D., and Rust, N.C. (2012). How Does the Brain Solve Visual Object Recognition? Neuron *73*, 415–434.

7. Squire, R.F., Noudoost, B., Schafer, R.J., and Moore, T. (2013). Prefrontal contributions to visual selective attention. Annual Review of Neuroscience *36*, 451–466.

8. Roelfsema, P.R. and de Lange, F.P. (2016). Early Visual Cortex as a Multiscale Cognitive Blackboard. Annual Review of Vision Science *2*, 131–151.

9. Bastos, A.M., Usrey, W.M., Adams, R.A., Mangun, G.R., Fries, P., and Friston, K.J. (2012). Canonical microcircuits for predictive coding. Neuron *76*, 695–711.

10. Lamme, V.A.F. and Roelfsema, P.R. (2000). The distinct modes of vision offered by feedforward and recurrent processing. Trends in Neurosciences *23*, 571–579.

11. Takahashi, N., Oertner, T.G., Hegemann, P., and Larkum, M.E. (2016). Active cortical dendrites modulate perception. Science *354*, 1587.

12. Larkum, M. (2013). A cellular mechanism for cortical associations: An organizing principle for the cerebral cortex. Trends in Neurosciences *36*, 141–151.

13. Heeger, D.J. (2017). Theory of cortical function. Proceedings of the National Academy of Sciences *114*, 1773–1782.

14. Gilbert, C.D. and Li, W. (2013). Top-down influences on visual processing. Nature Reviews Neuroscience *14*, 350–63.

15. Sherman, S.M. and Guillery, R.W. (2002). The role of the thalamus in the flow of information to the cortex. Philosophical Transactions of the Royal Society B: Biological Sciences *357*, 1695–708.

16. Briggs, F. (2010). Organizing principles of cortical layer 6. Frontiers in Neural Circuits *4*, 3.

17. Sillito, A.M. and Jones, H.E. (2002). Corticothalamic interactions in the transfer of visual information. Philosophical Transactions of the Royal Society of London B: Biological Sciences *357*, 1739–1752.

18. Vélez-Fort, M., Rousseau, C.V., Niedworok, C.J., Wickersham, I.R., Rancz, E.A., Brown, A.P.Y., Strom, M., and Margrie, T.W. (2014). The stimulus selectivity and connectivity of layer six principal cells reveals cortical microcircuits underlying visual processing. Neuron *83*, 1431–43.

19. Stoelzel, C.R., Bereshpolova, Y., Alonso, J.M., and Swadlow, H.A. (2017). Axonal Conduction Delays, Brain State, and Corticogeniculate Communication. Journal of Neuroscience *37*, 6342–6358.

20. Crandall, S.R., Patrick, S.L., Cruikshank, S.J., and Connors, B.W. (2017). Infrabarrels Are Layer 6 Circuit Modules in the Barrel Cortex that Link Long-Range Inputs and Outputs. Cell Reports *21*, 3065–3078.

21. Oberlaender, M., de Kock, C.P.J., Bruno, R.M., Ramirez, A., Meyer, H.S., Dercksen, V.J., Helmstaedter, M., and Sakmann, B. (2012). Cell Type–Specific Three-Dimensional Structure of Thalamocortical Circuits in a Column of Rat Vibrissal Cortex. Cerebral Cortex *22*, 2375–2391.

22. Swadlow, H.A. (1989). Efferent neurons and suspected interneurons in S-1 vibrissa cortex of the awake rabbit: Receptive fields and axonal properties. Journal of Neurophysiology *62*, 288–308.

23. Pauzin, F.P. and Krieger, P. (2018). A Corticothalamic Circuit for Refining Tactile Encoding. Cell Reports *23*, 1314–1325.

24. Andermann, M.L., Gilfoy, N.B., Goldey, G.J., Sachdev, R.N.S., Wölfel, M., McCormick, D.A., Reid, R.C., and Levene, M.J. (2013). Chronic cellular imaging of entire cortical columns in awake mice using microprisms. Neuron *80*, 900–13.

25. Denman, D.J. and Contreras, D. (2015). Complex effects on in vivo visual responses by specific projections from mouse cortical layer 6 to dorsal lateral geniculate nucleus. J Neurosci *35*, 9265–9280.

26. Sherman, S.M. and Guillery, R.W. (1998). On the actions that one nerve cell can have on another: Distinguishing "drivers" from "modulators". Proceedings of the National Academy of Sciences *95*, 7121–7126.

27. Godwin, D.W., Horn, S.C.V., Erişir, A., Sesma, M., Romano, C., and Sherman, S.M. (1996). Ultrastructural Localization Suggests that Retinal and Cortical Inputs Access Different Metabotropic Glutamate Receptors in the Lateral Geniculate Nucleus. Journal of Neuroscience *16*, 8181–8192.

28. Usrey, M.W. and Murray, S.S. (2018). Corticofugal circuits: Communication lines from the cortex to the rest of the brain. Journal of Comparative Neurology *0*.

29. Crandall, S.R., Cruikshank, S.J., and Connors, B.W. (2015). A corticothalamic switch: controlling the thalamus with dynamic synapses. Neuron *86*, 768–782.

30. Briggs, F. and Usrey, W.M. (2008). Emerging views of corticothalamic function. Curr Opin Neurobiol *18*, 403–407.

31. Briggs, F. and Usrey, W.M. (2011). Corticogeniculate feedback and visual processing in the primate. Journal of Physiology *589*, 33–40.

32. Andolina, I.M., Jones, H.E., and Sillito, A.M. (2013). Effects of cortical feedback on the spatial properties of relay cells in the lateral geniculate nucleus. Journal of Neurophysiology *109*, 889–899.

33. Cudeiro, J. and Sillito, A.M. (1996). Spatial frequency tuning of orientation-discontinuity-sensitive corticofugal feedback to the cat lateral geniculate nucleus. The Journal of Physiology *490 (Pt 2)*, 481–492.

34. Murphy, P.C. and Sillito, A.M. (1987). Corticofugal feedback influences the generation of length tuning in the visual pathway. Nature *329*, 727.

35. Webb, B.S., Tinsley, C.J., Barraclough, N.E., Easton, A., Parker, A., and Derrington, A.M. (2002). Feedback from V1 and inhibition from beyond the classical receptive field modulates the responses of neurons in the primate lateral geniculate nucleus. Visual Neuroscience *19*, 583–592.

36. Nolt, M.J., Kumbhani, R.D., and Palmer, L.A. (2007). Suppression at High Spatial Frequencies in the Lateral Geniculate Nucleus of the Cat. J Neurophysiol *98*, 1167–1180.

37. Hasse, J.M. and Briggs, F. (2017). Corticogeniculate feedback sharpens the temporal precision and spatial resolution of visual signals in the ferret. Proceedings of the National Academy of Sciences *114*, E6222–E6230.

38. Rivadulla, C., Martínez, L.M., Varela, C., and Cudeiro, J. (2002). Completing the corticofugal loop: A visual role for the corticogeniculate type 1 metabotropic glutamate receptor. Journal of Neuroscience *22*, 2956–2962.

39. Jones, H.E., Andolina, I.M., Ahmed, B., Shipp, S.D., Clements, J.T.C., Grieve, K.L., Cudeiro, J., Salt, T.E., and Sillito, A.M. (2012). Differential feedback modulation of center and surround mechanisms in parvocellular cells in the visual thalamus. The Journal of Neuroscience: The Official Journal of the Society for Neuroscience *32*, 15946–15951.

40. Andolina, I.M., Jones, H.E., Wang, W., and Sillito, A.M. (2007). Corticothalamic feedback enhances stimulus response precision in the visual system. Proceedings of the National Academy of Sciences of the United States of America *104*, 1685–1690.

41. Olsen, S.R., Bortone, D.S., Adesnik, H., and Scanziani, M. (2012). Gain control by layer six in cortical circuits of vision. Nature *483*, 47.

42. Przybyszewski, A.W., Gaska, J.P., Foote, W., and Pollen, D.A. (2000). Striate cortex increases contrast gain of macaque LGN neurons. Visual Neuroscience *17*, 485–494.

43. Wörgötter, F., Eyding, D., Macklis, J.D., and Funke, K. (2002). The influence of the corticothalamic projection on responses in thalamus and cortex. Philosophical Transactions of the Royal Society of London. Series B: Biological Sciences *357*, 1823–1834.

44. Wang, W., Jones, H.E., Andolina, I.M., Salt, T.E., and Sillito, A.M. (2006). Functional alignment of feedback effects from visual cortex to thalamus. Nat Neurosci *9*, 1330.

45. de Labra, C., Rivadulla, C., Grieve, K., Mariño, J., Espinosa, N., and Cudeiro, J. (2007). Changes in Visual Responses in the Feline dLGN: Selective Thalamic Suppression Induced by Transcranial Magnetic Stimulation of V1. Cerebral Cortex *17*, 1376–1385.

46. Li, Y.T., Ibrahim, L.A., Liu, B.H., Zhang, L.I., and Tao, H.W. (2013). Linear transformation of thalamocortical input by intracortical excitation. Nature Neuroscience *16*, 1324–30.

47. Lien, A.D. and Scanziani, M. (2013). Tuned thalamic excitation is amplified by visual cortical circuits. Nature Neuroscience *16*, 1315–23.

48. King, J.L., Lowe, M.P., Stover, K.R., Wong, A.A., and Crowder, N.A. (2016). Adaptive Processes in Thalamus and Cortex Revealed by Silencing of Primary Visual Cortex during Contrast Adaptation. Current biology *26*, 1295–1300.

49. Gulyás, B., Lagae, L., Eysel, U., and Orban, G.A. (1990). Corticofugal feedback influences the responses of geniculate neurons to moving stimuli. Experimental Brain Research *79*, 441–446.

50. Poltoratski, S., Maier, A., Newton, A.T., and Tong, F. (2019). Figure-Ground Modulation in the Human Lateral Geniculate Nucleus Is Distinguishable from Top-Down Attention. Current Biology *29*, 2051–2057.e3.

51. Makino, H. and Komiyama, T. (2015). Learning enhances the relative impact of top-down processing in the visual cortex. Nature Neuroscience *18*, 1116–1122.

52. Atallah, B.V., Bruns, W., Carandini, M., and Scanziani, M. (01 2012/01/12). Parvalbumin-Expressing Interneurons Linearly Transform Cortical Responses to Visual Stimuli. Neuron *73*, 159–170.

53. Sherman, S.M. (2016). Thalamus plays a central role in ongoing cortical functioning. Nat Neurosci *19*, 533–541.

54. Vinje, W.E. and Gallant, J.L. (2000). Sparse coding and decorrelation in primary visual cortex during natural vision. Science *287*, 1273–1276.

55. Goard, M. and Dan, Y. (2009). Basal forebrain activation enhances cortical coding of natural scenes. Nat Neurosci *12*, 1444–1449.

833 56. Sherman, S.M. (2001). Tonic and burst firing: dual modes of thalamocortical relay.
834 Trends Neurosci *24*, 122–126.

835 57. Piscopo, D.M., El-Danaf, R.N., Huberman, A.D., and Niell, C.M. (2013). Diverse visual
836 features encoded in mouse lateral geniculate nucleus. Journal of Neuroscience *33*, 4642–
837 56.

838 58. Román Rosón, M., Bauer, Y., Kotkat, A.H., Berens, P., Euler, T., and Busse, L. (2019).
839 Mouse dLGN Receives Functional Input from a Diverse Population of Retinal Ganglion
840 Cells with Limited Convergence. Neuron *0*.

841 59. Marshel, J.H., Kaye, A.P., Nauhaus, I., and Callaway, E.M. (2012). Anterior-posterior
842 direction opponency in the superficial mouse lateral geniculate nucleus. Neuron *76*,
843 713–20.

844 60. Scholl, B., Tan, A.Y.Y., Corey, J., and Priebe, N.J. (2013). Emergence of orientation
845 selectivity in the Mammalian visual pathway. Journal of Neuroscience *33*, 10616–24.

846 61. Skottun, B.C., De Valois, R.L., Grosof, D.H., Movshon, J.A., Albrecht, D.G., and
847 Bonds, A.B. (1991). Classifying simple and complex cells on the basis of response
848 modulation. Vision Research *31*, 1079–1086.

849 62. Carandini, M., Heeger, D.J., and Movshon, J.A. (1997). Linearity and Normalization
850 in Simple Cells of the Macaque Primary Visual Cortex. Journal of Neuroscience *17*,
851 8621–8644.

852 63. Erisken, S., Vaiceliunaite, A., Jurjut, O., Fiorini, M., Katzner, S., and Busse, L. (2014).
853 Effects of Locomotion Extend throughout the Mouse Early Visual System. Current
854 Biology *24*, 2899–2907.

855 64. Aydın, Ç., Couto, J., Giugliano, M., Farrow, K., and Bonin, V. (2018). Locomotion
856 modulates specific functional cell types in the mouse visual thalamus. Nature Commu-
857 nications *9*, 4882.

858 65. Williamson, R.S., Hancock, K.E., Shinn-Cunningham, B.G., and Polley, D.B. (2015).
859 Locomotion and Task Demands Differentially Modulate Thalamic Audiovisual Process-
860 ing during Active Search. Current Biology *25*, 1885–1891.

861 66. Niell, C.M. and Stryker, M.P. (02 2010/02/25). Modulation of Visual Responses by
862 Behavioral State in Mouse Visual Cortex. Neuron *65*, 472–479.

863 67. Bennett, C., Arroyo, S., and Hestrin, S. (10 2013/10/16). Subthreshold Mechanisms
864 Underlying State-Dependent Modulation of Visual Responses. Neuron *80*, 350–357.

865 68. Wiegert, J.S., Mahn, M., Prigge, M., Printz, Y., and Yizhar, O. (2017). Silencing
866 Neurons: Tools, Applications, and Experimental Constraints. Neuron *95*, 504–529.

867 69. Mahn, M., Gibor, L., Patil, P., Malina, K.C.K., Oring, S., Printz, Y., Levy, R., Lampl,
868 I., and Yizhar, O. (2018). High-efficiency optogenetic silencing with soma-targeted
869 anion-conducting channelrhodopsins. Nature Communications *9*, 4125.

70. Bickford, M.E., Zhou, N., Krahe, T.E., Govindaiah, G., and Guido, W. (2015). Retinal and Tectal "Driver-Like" Inputs Converge in the Shell of the Mouse Dorsal Lateral Geniculate Nucleus. Journal of Neuroscience *35*, 10523–10534.

71. Ahmadlou, M., Tafreshiha, A., and Heimel, J.A. (2017). Visual Cortex Limits Pop-Out in the Superior Colliculus of Awake Mice. Cerebral Cortex *27*, 5772–5783.

72. Zhao, X., Liu, M., and Cang, J. (2014). Visual Cortex Modulates the Magnitude but Not the Selectivity of Looming-Evoked Responses in the Superior Colliculus of Awake Mice. Neuron *84*, 202–213.

73. Ahmadlou, M., Zweifel, L.S., and Heimel, J.A. (2018). Functional modulation of primary visual cortex by the superior colliculus in the mouse. Nature Communications *9*, 3895.

74. Dan, Y., Atick, J.J., and Reid, R.C. (1996). Efficient coding of natural scenes in the lateral geniculate nucleus: experimental test of a computational theory. J Neurosci *16*, 3351–3362.

75. Lesica, N.A. and Stanley, G.B. (2004). Encoding of Natural Scene Movies by Tonic and Burst Spikes in the Lateral Geniculate Nucleus. Journal of Neuroscience *24*, 10731–10740.

76. Lesica, N.A., Weng, C., Jin, J., Yeh, C.I., Alonso, J.M., and Stanley, G.B. (2006). Dynamic Encoding of Natural Luminance Sequences by LGN Bursts. PLoS Biology *4*.

77. Wang, X., Wei, Y., Vaingankar, V., Wang, Q., Koepsell, K., Sommer, F.T., and Hirsch, J.A. (2007). Feedforward Excitation and Inhibition Evoke Dual Modes of Firing in the Cat's Visual Thalamus during Naturalistic Viewing. Neuron *55*, 465–478.

78. Mante, V., Frazor, R.A., Bonin, V., Geisler, W.S., and Carandini, M. (2005). Independence of luminance and contrast in natural scenes and in the early visual system. Nature Neuroscience *8*, 1690–1697.

79. Berkes, P., Orbán, G., Lengyel, M., and Fiser, J. (01 2011/01/07). Spontaneous Cortical Activity Reveals Hallmarks of an Optimal Internal Model of the Environment. Science *331*, 83–87.

80. Lee, T.S. and Mumford, D. (2003). Hierarchical Bayesian inference in the visual cortex. JOSA A *20*, 1434–1448.

81. Rao, R.P.N. and Ballard, D.H. (1999). Predictive coding in the visual cortex: A functional interpretation of some extra-classical receptive-field effects. Nature Neuroscience *2*, 79.

82. Clark, A. (2013). Whatever next? Predictive brains, situated agents, and the future of cognitive science. Behavioral and Brain Sciences *36*, 181–204.

83. Mobarhan, M.H., Halnes, G., Martínez-Cañada, P., Hafting, T., Fyhn, M., and Einevoll, G.T. (2018). Firing-rate based network modeling of the dLGN circuit: Effects of cortical feedback on spatiotemporal response properties of relay cells. PLOS Computational Biology *14*, e1006156.

84. Jahnsen, H. and Llinás, R. (1984). Voltage-dependent burst-to-tonic switching of thalamic cell activity: An in vitro study. Archives Italiennes De Biologie *122*, 73–82.

85. Dossi, R.C., Nuñez, A., and Steriade, M. (1992). Electrophysiology of a slow (0.5-4 Hz) intrinsic oscillation of cat thalamocortical neurones in vivo. The Journal of Physiology *447*, 215–234.

86. Mease, R.A., Krieger, P., and Groh, A. (2014). Cortical control of adaptation and sensory relay mode in the thalamus. Proceedings of the National Academy of Sciences *111*, 6798–6803.

87. Alitto, H., Rathbun, D.L., Vandeleest, J.J., Alexander, P.C., and Usrey, W.M. (2019). The Augmentation of Retinogeniculate Communication during Thalamic Burst Mode. Journal of Neuroscience *39*, 5697–5710.

88. Swadlow, H.A. and Gusev, A.G. (2001). The impact of 'bursting' thalamic impulses at a neocortical synapse. Nature Neuroscience *4*, 402–408.

89. Guido, W., Lu, S.M., Vaughan, J.W., Godwin, D.W., and Sherman, S.M. (1995). Receiver operating characteristic (ROC) analysis of neurons in the cat's lateral geniculate nucleus during tonic and burst response mode. Visual Neuroscience *12*, 723–741.

90. Mease, R.A., Kuner, T., Fairhall, A.L., and Groh, A. (2017). Multiplexed Spike Coding and Adaptation in the Thalamus. Cell Reports *19*, 1130–1140.

91. Guo, W., Clause, A.R., Barth-Maron, A., and Polley, D.B. (2017). A Corticothalamic Circuit for Dynamic Switching between Feature Detection and Discrimination. Neuron *95*, 180–194.e5.

92. Murata, Y. and Colonnese, M.T. (2018). Thalamus Controls Development and Expression of Arousal States in Visual Cortex. Journal of Neuroscience *38*, 8772–8786.

93. Grubb, M.S. and Thompson, I.D. (2003). Quantitative Characterization of Visual Response Properties in the Mouse Dorsal Lateral Geniculate Nucleus. Journal of Neurophysiology *90*, 3594–3607.

94. Rueden, C.T., Schindelin, J., Hiner, M.C., DeZonia, B.E., Walter, A.E., Arena, E.T., and Eliceiri, K.W. (2017). ImageJ2: ImageJ for the next generation of scientific image data. BMC Bioinformatics *18*.

95. Schindelin, J., Arganda-Carreras, I., Frise, E., Kaynig, V., Longair, M., Pietzsch, T., Preibisch, S., Rueden, C., Saalfeld, S., Schmid, B., et al. (2012). Fiji: An open-source platform for biological-image analysis. Nature Methods *9*, 676–682.

96. Poynton, C.A. (1998). Rehabilitation of gamma, in Human Vision and Electronic Imaging III, B.E. Rogowitz and T.N. Pappas, eds., volume 3299 (San Jose, CA: International Society for Optical Engineering), pp. 232–249.

97. Pachitariu, M., Steinmetz, N.A., Kadir, S.N., Carandini, M., and Harris, K.D. (2016). Fast and accurate spike sorting of high-channel count probes with KiloSort, in Advances in Neural Information Processing Systems 29, D.D. Lee, M. Sugiyama, U.V. Luxburg, I. Guyon, and R. Garnett, eds. (Curran Associates, Inc.), pp. 4448–4456.

98. Spacek, M.A., Blanche, T.J., and Swindale, N.V. (2009). Python for large-scale electrophysiology. Front Neuroinform *2*, 9.

99. Swindale, N.V. and Spacek, M.A. (2014). Spike sorting for polytrodes: a divide and conquer approach. Front Syst Neurosci *8*, 6.

100. Yatsenko, D., Walker, E.Y., and Tolias, A.S. (2018). DataJoint: A simpler relational data model. arXiv *1807*, 11104.

101. Mitzdorf, U. (1985). Current source-density method and application in cat cerebral cortex: Investigation of evoked potentials and EEG phenomena. Physiological Reviews *65*, 37–100.

102. Heumann, D., Leuba, G., and Rabinowicz, T. (1977). Postnatal development of the mouse cerebral neocortex. II. Quantitative cytoarchitectonics of visual and auditory areas. Journal Fur Hirnforschung *18*, 483–500.

103. van der Togt, C., Spekreijse, H., and Supèr, H. (2005). Neural responses in cat visual cortex reflect state changes in correlated activity. European Journal of Neuroscience *22*, 465–475.

104. Baden, T., Berens, P., Franke, K., Román Rosón, M., Bethge, M., and Euler, T. (01 2016/01/21/print). The functional diversity of retinal ganglion cells in the mouse. Nature *529*, 345–350.

105. Bonhoeffer, T., Kim, D.S., Malonek, D., Shoham, D., and Grinvald, A. (1995). Optical Imaging of the Layout of Functional Domains in Area 17 and Across the Area 17/18 Border in Cat Visual Cortex. European Journal of Neuroscience *7*, 1973–1988.

106. Remtulla, S. and Hallett, P. (1985). A schematic eye for the mouse, and comparisons with the rat. Vision research *25*, 21–31.

107. Gelman, A. and Hill, J. (2007). Data Analysis Using Regression and Multilevel/Hierarchical Models, Analytical Methods for Social Research (Cambridge ; New York: Cambridge University Press), oCLC: ocm67375137.

108. Aarts, E., Verhage, M., Veenvliet, J.V., Dolan, C.V., and van der Sluis, S. (2014). A solution to dependency: Using multilevel analysis to accommodate nested data. Nature Neuroscience *17*, 491–496.

977 109. R Core Team (2017). R: A Language and Environment for Statistical Computing, R
978 Foundation for Statistical Computing, Vienna, Austria.

979 110. Bates, D., Mächler, M., Bolker, B., and Walker, S. (2015). Fitting Linear Mixed-Effects
980 Models Using **lme4**. Journal of Statistical Software *67*.

981 111. Luke, S.G. (2017). Evaluating significance in linear mixed-effects models in R. Behavior
982 Research Methods *49*, 1494–1502.

983 112. Kuznetsova, A., Brockhoff, P.B., and Christensen, R.H.B. (2017). **lmerTest** Package:
984 Tests in Linear Mixed Effects Models. Journal of Statistical Software *82*.

Supplementary Information

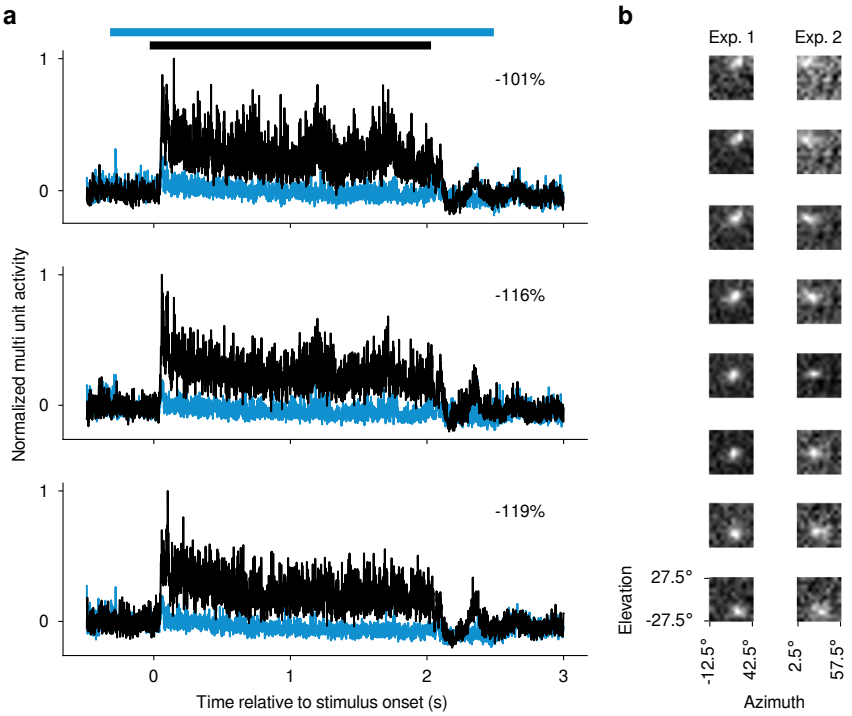

Figure S1 Confirmation of optogenetic suppression of V1 responses and targeting dLGN for recordings. (**a**) MUAe responses [103] to 2 s drifting gratings recorded in one experiment for three example channels. All three channels were located, as determined by current source density analysis [101], in the infragranular layers of V1. *Black*: Mean MUAe responses across control trials; *blue*: MUAe responses in trials with optogenetic activation of PV+ inhibitory interneurons. Normalized MUAe was computed by subtracting the mean activity across both conditions in a 200 ms time window prior to light onset before normalizing to the maximum response across the two conditions. Percentages indicate mean reduction in MUAe over the stimulus presentation period. *Black bar*: stimulus period; *blue bar*: photoactivation period. (**b**) MUAe-based RFs for channels located in dLGN during two example RF mapping experiments. Each panel represents one channel, with the top channel being located most dorsally and the bottom channel most ventrally in the dLGN. RFs were computed as the mean response to a change in contrast at a given monitor position in a time window ranging from 50 ms after stimulus onset to 100 ms after stimulus offset. Brighter pixels indicate higher activity. The emerging characteristic pattern with more ventrally located channels representing locations lower in the visual field was used to confirm successful targeting of dLGN.

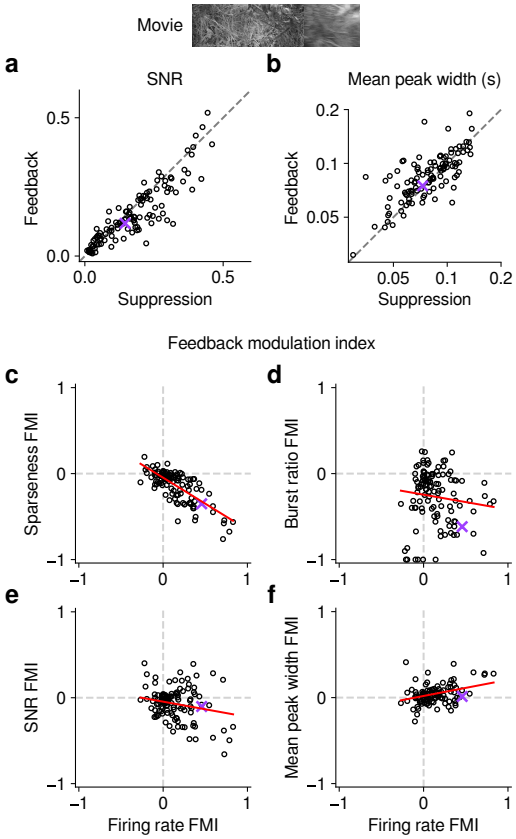

Figure S2 Effects of CT feedback on additional parameters of responses to naturalistic movies and relationship with firing rate.
(**a, b**) Comparison of CT feedback vs. V1 suppression conditions for PSTH signal-to-noise ratio (SNR) (a) and mean peak width (b). SNR was computed as in [104], and compares the variance of the trial-averaged PSTH across time relative to the single-trial variance across time, averaged across stimulus repeats. If all trials are identical such that the PSTH is a perfect representation of the each trial's response, SNR equals 1. The width of PSTH peaks that exceeded a threshold amplitude was measured as the temporal separation of the middle 68% of spikes clustered as part of each peak (see Methods). Narrow peaks are a proxy for high temporal precision of responses. With CT feedback intact, mean SNR was lower (0.14 vs. 0.16, LMM: $F_{1,154.7} = 14.72$, $p = 0.00018$) and mean peak width was higher (0.086 vs. 0.080, LMM: $F_{1,153} = 7.0$, $p = 0.0088$). (**c–f**) Relationship between CT feedback effects (FMI) on firing rate and sparseness (c), burst ratio (d), SNR (e), and peak width (f). CT feedback-related changes in firing rate can to a large degree account for the changes in sparseness (LMM: slope of -0.60 ± 0.11; (c)). For all other measures, slopes were either non-significant or closer to 0 (Burst ratio, LMM: slope of -0.17 ± 0.29; SNR, LMM: slope of -0.18 ± 0.18; peak width, LMM: slope of 0.19 ± 0.11).

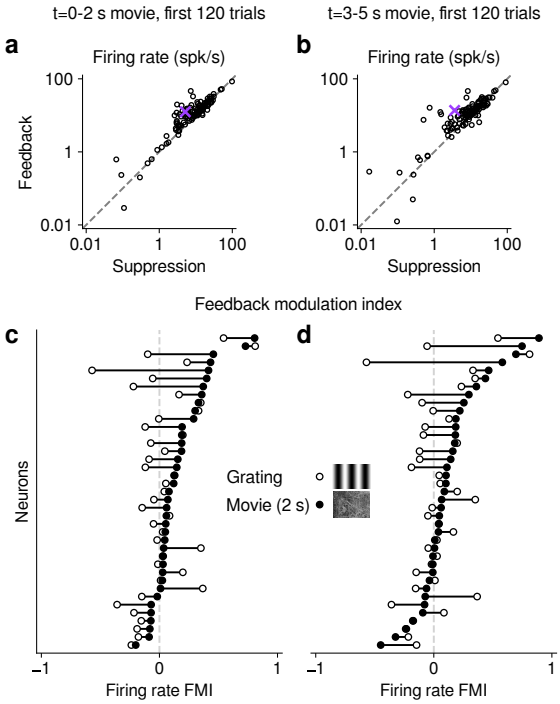

Figure S3 Comparison of effects of V1 suppression for different parts of the naturalistic movie clips and for the first 120 trials only.
(**a, b**) In conditions with CT feedback intact, dLGN firing rates were consistently higher than during V1 suppression, both for the first 2 s (a) and the last 2 s (b) of the movie clips (main effect of feedback, LMM: $F_{1,394.9} = 14.6$, $p = 0.00015$), and the effect of V1 suppression was indistinguishable during the first two and the last two seconds of the movie clips (interaction feedback × analysis window, LMM: $F_{1,394.9} = 0.61$, $p = 0.43$). Higher consistency of effects of V1 feedback suppression on firing rates to naturalistic movies thus cannot be explained by the longer duration of the movies (5 s) compared to gratings (2 s). (**c, d**) Comparison of feedback modulation index (FMI) of firing rates for gratings vs. movies, separately for the first 2 s (c) and the last 2 s (d) of the movie clips. Firing rate FMIs were significantly more positive for movies vs. gratings, even when considering only the first 2 s (mean FMI of 0.16 (movies) vs. 0.022 (gratings); LMM: $F_{1,38} = 12.7$, $p = 0.00099$) (c). Considering only the last 2 s of the movies (d) gave very similar results (mean FMI of 0.14 (movies) vs. 0.03 (gratings); LMM: $F_{1,38} = 5.7$, $p = 0.022$). Hence, even when we limited our analysis to the first 2 s of the movie clips, CT feedback effects remained stronger for movies than gratings. Together, these analyses show that considering the full 5 s of the movie clips does not inflate the difference in firing rate FMI between movies and gratings, but is rather a conservative estimate of the effect.

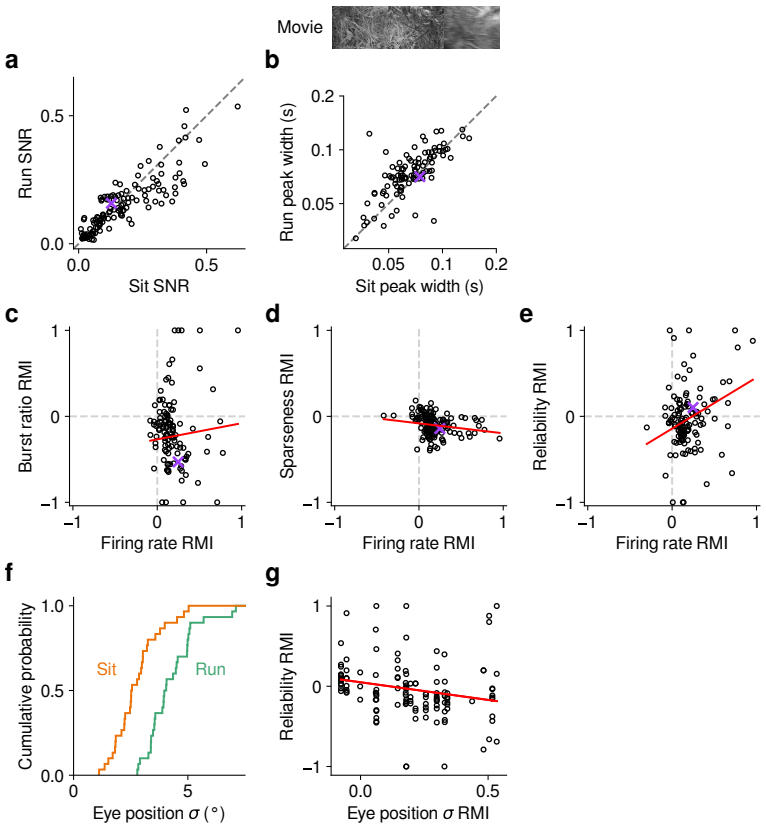

Figure S4 Effects of locomotion on additional parameters of responses to naturalistic movie clips and relationship with firing rate.
(**a,b**) Comparison between trials with locomotion and stationary periods for (a) SNR [104] and (b) width of response peaks. During locomotion, SNR is lower (0.14 vs. 0.16, LMM: $F_{1,190.4} = 4.9$, $p = 0.029$) and peak width broader (0.075 vs. 0.068, LMM: $F_{1,146.2} = 13.1$, $p = 0.00040$). (**c–e**) Relationship between locomotion effects (RMI) on firing rate vs. burst ratio (c), sparseness (d), and reliability (e). Locomotion-related changes in firing rate can to some degree account for the changes in reliability (LMM: slope of 0.59 ± 0.38; (e)). For all other measures, slopes were non-significant (Burst ratio, LMM: slope of 0.19 ± 0.43; sparseness, LMM: slope of -0.12 ± 0.12). (**f**) Distribution of trial-averaged eye-position standard deviation for trials with locomotion (*green*) and stationary periods (*orange*). Eye-position standard deviation was first calculated for each time point across trials, and then averaged across time points. In line with previous reports [63, 67], standard deviation of eye position was, on average, larger during locomotion than during stationary periods (4.27° vs. 2.76°, LMM: $F_{1,49} = 53.6.5$, $p = 2.1 \times 10^{-9}$, $N = 30$ experiments from 6 mice). (**g**) Locomotion-related trial-to-trial reliability co-varied with locomotion-related changes in eye position standard deviation (LMM: slope of -0.44 ± 0.36); however, the expected difference in reliability RMI corresponding to a 1 standard deviation difference in eye position σ RMI is -0.081, which is much smaller than the residual standard deviation of 0.28 unexplained by the regression. Therefore, changes in eye position during locomotion cannot reliably account for the reduced reliability of responses during locomotion (**Fig. 5f**).

Figure S5 Two example movies used for the recordings.